THE ASTROPHYSICAL JOURNAL, 343:785–810, 1989 August 15

VELOCITIES AND ROTATIONAL EXCITATION OF INTERSTELLAR H_2 TOWARD π SCORPII

EDWARD B. JENKINS, JOANNA F. LEES, EWINE F. VAN DISHOECK, AND ERIC M. WILCOTS
Princeton University Observatory
Received 1988 October 18; accepted 1989 January 25

ABSTRACT

A spectrum of π Sco with continuous coverage from 1003 to 1172 Å and a resolution $\lambda/\Delta\lambda \geq 1.3 \times 10^5$ was recorded by an objective-grating echelle spectrograph on a sounding rocket. In addition to numerous atomic lines the spectrum shows 70 absorption features from the Lyman and Werner transitions of interstellar H_2 in rotational levels $J = 0$ to $J = 5$. Initially, for $J = 3$, 4, and 5 and part of the $J = 2$ profile, we assumed that the absorption profiles were perfectly resolved and derived optical depths as a function of velocity from lines of differing strength. In turn, for each J level we constructed composite column density profiles after we normalized the optical depths according to line strength and superposed them. In the best cases, such profiles covered a dynamic range of 100. The profiles for all J levels are centered at a heliocentric velocity of -17.4 km s^{-1} and show no systematic velocity difference in excess of 1 km s^{-1} with increasing J. Their shapes are very nearly Gaussian with a one-dimensional rms velocity dispersion $\sigma \simeq 3$ km s^{-1}, but with a slight decrease in σ going from low to high J.

From small, systematic differences in the inferred $N(H_2)$ as a function of velocity reconstructed from strong and weak lines, we conclude that, contrary to our initial assumptions, not all of the structures in the profiles for various J levels were resolved by the instrument. The behavior of the shifts is consistent with the overall profiles being composed of nearly symmetrical, tightly packed assemblies of about seven unresolved components. Each component has a width about as narrow as that arising from pure thermal Doppler broadening ($b \simeq 0.8$ km s^{-1}).

The relative overall column densities in the higher J levels of H_2 are consistent with a theoretical model where these states are populated by optical pumping through the Lyman and Werner transitions, powered by ultraviolet radiation from nearby stars which create a flux approximately 4 times the mean interstellar value. To explain the slight narrowing of the high-J profiles, we propose that small clumps of H_2 at radial velocities some 5–8 km s^{-1} from the core of the profile seem to be exposed to a pumping flux roughly 10 times lower than that for the (low-velocity) material near the profile's center. In a simple picture where all of the H_2 is in one general location, we envision a swarm of cloudlets where the more rapidly moving parcels are confined to the center and are thus shielded by the H_2 absorption line opacity of the surrounding material. There is evidence that a shock may have overtaken the clouds several million years ago; this event may have created and subsequently dispersed high-velocity clouds at the edge, but such clouds may still be trapped in the center of the complex by the overlying, low-velocity material.

Subject headings: interstellar: molecules — stars: individual (π Sco) — ultraviolet: spectra

I. BACKGROUND

From 1972 to 1980, the spectrometer on the *Copernicus* satellite recorded far-ultraviolet spectra of hot stars, yielding a vast array of important absorption features arising from the interstellar medium. Many of these lines gave us our first insights on the abundances, ionization, kinematics, and excitation of certain atoms and molecules in space. Technological advances in UV photon sensors now allow us to operate with an enormous improvement in efficiency over the scanning photomultipliers assembled for *Copernicus* in the late 1960s; with a small instrument aboard a sounding rocket, we return to the lucrative spectral region below 1150 Å to study in greater detail the broad assortment of H_2 and atomic lines.

In the *Copernicus* era, the absorption lines in the Lyman and Werner systems of H_2 were exploited to indicate not only how much of this most abundant molecule in space is present (Bohlin, Savage, and Drake 1978) but also the relative occupations in different rotational states (Spitzer and Cochran 1973; Spitzer, Cochran, and Hirshfeld 1974; Morton 1975; Morton and Dinerstein 1976). These populations indicated local gas densities and temperatures and the rate of ultraviolet pumping of rotational levels (Black and Dalgarno 1973, 1977; Spitzer and Zweibel 1974; Jura 1975*a*, *b*). In some contexts, the presence of absorptions from excited J levels with small velocity displacements can signal the energizing of H_2 by interstellar shocks (Aannestad and Field 1973; Draine and Katz 1986).

Spitzer and Morton (1976) pushed very near the limits of attainable signal quality of *Copernicus* in a concerted effort to unravel the velocity structure within the instrumentally blended profiles of the higher rotation lines of H_2. Their goal was to differentiate between two proposed explanations for the slight increases in line width with higher J noted earlier by Spitzer, Cochran, and Hirshfeld (1974) for H_2 near very luminous stars. On the one hand, newly created H_2 molecules might have much of their formation energy converted to large translational and rotational energy as they left the grains. Since high-J molecules have relatively short radiative lifetimes, they cannot couple by collisions with other particles. Hence their large random velocities would be preserved, and their contributions on top of radiatively pumped molecules would lead to a simple broadening of the absorption, when compared with the lower J profiles. On the other hand, contributions of

shock-excited molecules to the quiescent high-J H_2 would produce, in most instances, a velocity *shift* in addition to the broadening. The data of Spitzer and Morton did indeed show such shifts, thus supporting the latter interpretation.

An important motivation for studying the absorption lines of H_2 at higher resolution is to investigate more carefully the changes in velocity structure with J, since the effect studied earlier was at the threshold of detectability for *Copernicus*. Snow, McClintock, and Voels (1988) used a sounding-rocket payload to record some Lyman band absorptions toward δ Sco with a resolving power in wavelength superior to that of *Copernicus*, and they found no velocity shifts for different J (their signal quality was not sufficient to measure small differences in width). To investigate the issue still further, we recorded a spectrum of π Sco at an even higher velocity resolution. To our surprise, the data indicate a progression of velocity widths with increasing J which runs opposite to the trend found in the earlier investigations, i.e., the lines become slightly *narrower* for higher rotational excitations (see § IV*f*). This finding, along with evidence for a clumpy structure in the gas (§ IV*d*), forces us to consider an entirely different theoretical interpretation (§ V) based on changes in the optical pumping rates for different parcels of gas. Atomic lines observed in our spectrum of π Sco are only mentioned in passing (§ III*f*); a detailed treatment will be given in a subsequent paper.

II. SPECTROGRAPH PAYLOAD

The H_2 profiles toward π Sco were recorded by the Interstellar Medium Absorption Profile Spectrograph (IMAPS) sounding-rocket payload. This instrument is an objective-grating, echelle spectrograph which was configured to record a far-UV spectrum of a point source at a resolving power roughly 10 times that obtained by the high-resolution scanning photomultiplier (U1) in the spectrograph of the *Copernicus* satellite. We summarize below the basic properties of IMAPS and how it operates; a far more detailed discussion has been presented by Jenkins *et al.* (1988).

A principal feature of the instrument's design is that it has only two reflecting surfaces and contains no transmission elements in either the optical train or the detector. This simple, all-reflective configuration allowed IMAPS to function with good efficiency in the wavelength region of the H_2 Lyman and Werner absorption lines. The optical layout is illustrated in Figure 1, and Table 1 lists some fundamental instrumental parameters.

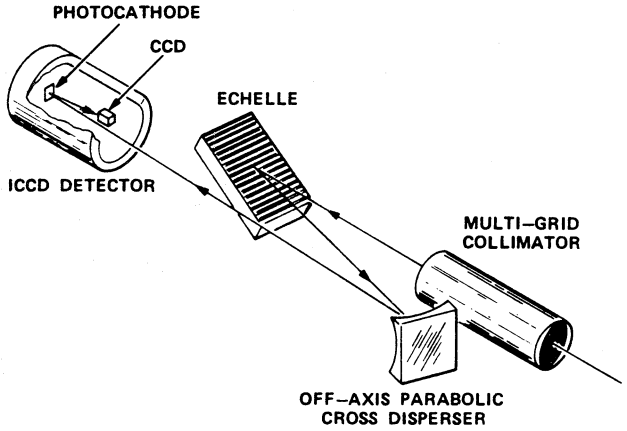

FIG. 1.—Schematic depiction of the IMAPS optical design. A mechanical collimator with a stack of grids containing a waffle pattern of apertures restricted the field of view to 1°. The large incidence angle of the echelle (63°) and long focal length of the cross-disperser (1800 mm) result in a high dispersion in the focal plane: each 30 μm pixel on the CCD subtends a $\Delta\lambda = \lambda/240{,}000$ (or a Doppler shift of 1.25 km s^{-1}).

The first element in the system is a mechanical collimator which uses a stack of grids to restrict the field of view to a 1° circle. This restriction is needed to eliminate confusion from nearby stars in the sky. After passing through the collimator, the parallel wave front from the target star hits the echelle grating and then is diffracted toward a focusing cross-disperser grating. An image of the spectrum is formed inside the detector on an opaque KBr photocathode which is on a smooth substrate 1.5 cm in diameter. A photocathode of this sort should have a quantum efficiency of about 70% in the wavelength range of interest (Carruthers and Opal 1985). Electrons emitted by the photocathode are accelerated by an 18 kV electrostatic field and focused magnetically within the detector's image section, whereupon they directly bombard a thinned, back-illuminated CCD. Each electron impact creates several thousand secondary electrons which enable the single photoevents to be identified when the CCD signal is read out.

One dimension of the detector's active area gathers a sequence of echelle orders spread by the cross-disperser from

TABLE 1

INSTRUMENT PERFORMANCE PARAMETERS

Parameter	Value
Area of entrance aperture	250 cm^2
Effective area of the entire instrument (area of entrance aperture times the product of all component efficiencies)	3.8 cm^2
Image Format	320 × 256 30 μm CCD pixels (covers 18′20″ × 14′40″ of the sky)
Angle subtended by each pixel	3″.45
$\Delta\lambda$ subtended by each pixel	$\lambda/2.4 \times 10^5 = 1.25$ km s^{-1}
Free spectral range of each order	3.7 Å for $m = 238$ to 5.5 Å for $m = 197$
Order separation	122 μm for $m = 238$ to 178 μm for $m = 197$
Secondary electron yield for each photoevent	2500 electrons
rms readout noise in each pixel	75 electrons
Dark current at 20°C	3000 electrons in each 1/15 s frame
Maximum signal level accepted by the telemetry	8000 electrons[a]

[a] A special zero suppression of the signal prevents the dark current from consuming much of this dynamic range.

965 to 1175 Å, but the other dimension can span only one-fourth of the free spectral range of each order. To record a continuous spectrum, we needed to expose four frames in sequence, with a small change in the echelle grating's tilt angle for each exposure.

The CCD in the IMAPS detector is read out at a rate of 15 frames per second. Limitations in clocking pulse rise times, together with restricted bandwidths in the telemetry and recording equipment, prevented us from achieving higher frame rates. Figure 2 (Plate 34) shows one of the 4316 frames whose signals were co-added to produce the four final spectral images shown in Figure 3 (Plate 35). The complete CCD format of 256 lines, each with 320 pixels, was divided into 16 panels. This partitioning was a consequence of our requirement that the camera's signal conform to the standard broadcast TV signal protocol so that the telemetry receiver output could be recorded on an ordinary, consumer-grade video recorder during the flight. A single CCD frame required 2 standard TV frame signals (i.e., 4 interlaced fields) for a complete readout. Each broadcast line filled a line in one of the panels; the borders between the panels were caused by the pauses in readout during the horizontal and vertical retrace times in a standard TV signal.

Small mirrors (area ~ 1 cm^2) attached to the echelle grating direct light from the target star onto an unruled portion of the cross-disperser grating element. The beam of light is then focused on the lower portion of the detector format to create a bright, broad-band UV image of the star. For any single frame of data, this image serves as an instantaneous position reference for the spectrum and allows us to compensate for changes in rocket pointing ($\sim 1'$ amplitude) when the intensities were co-added from one frame to the next.

III. DATA

a) *Observations*

The spectrum of π Sco was obtained on NASA sounding-rocket mission 27.082 UG, which was launched on 1985 April 20 at 0750 UT (LST = 14^h38^m). At this time, π Sco was at a zenith angle of 66°. This star is a spectroscopic binary classified as B1 V + B2 V, and it has a visual magnitude of 2.88 and a $B-V$ color excess of 0.08. The launch was timed to occur near local midnight to minimize the diffuse background flux caused by the geocoronal Lyα emission. The payload was lofted to a peak altitude of 264 km by a Black Brant rocket with a Nike booster. The attitude control system acquired π Sco without difficulty, but for some of the time the stability was substantially worse than our specification of a maximum angular rate of 15″ per second of time. As a result, a small fraction of the data frames had an image smear with a slightly curtailed wavelength resolution. We obtained observing times of 69, 74, 90, and 54 s for the echelle tilt positions 1–4, respectively, shown in Figure 3. These observing intervals all occurred at an altitude greater than 120 km. The optimum blaze angle for the echelle grating was centered between positions 1 and 2, which accounts for the fact that position 4 is relatively faint (to a lesser extent, this also applies to position 3).

b) *Frame Signal Integrations*

After flight, each CCD image frame recorded on tape was digitized by having the video cassette recorder operate in a freeze-frame mode during playback. The signal from the recorder was sent to a Colorado Video digitizing and frame storage unit, which was connected to a VAX 8200 computer at Princeton. Some of the frames we recorded were transmitted before and after the detector's high voltage was activated on the flight. Appropriate averages of these frames were used as templates for the CCD dark current pattern and were subtracted from the active data frames before they were combined.

When the rocket pointing changes, the spectrum and the broad-band reference image move together. This similarity of movement is the result of the small angle of diffraction at the cross-disperser and our having the incidence and diffraction angles at the echelle equal.[1] After subtracting the dark current pattern, we added the frames in computer memory with x and y pixel address offsets which matched the respective locations of the reference star image. Instead of using the intensity centroid or median to indicate this position, we evaluated least-squares solutions for the offsets of the measured profiles with respect to very accurate template profiles of the star images. From short-term fluctuations in the perceived positions, we estimate that we achieved an accuracy of about $\frac{1}{2}$ CCD pixel or better. The spacing of intensity bins in the computer was $\frac{1}{2}$ pixel in x (along the echelle dispersion direction) and 1 pixel in y.

In addition to compensating for movement of the spectrum caused by changes in rocket pointing, we also artificially moved the x reference point with time, to correct for changes in the Doppler shifts of the lines caused by the projection along the line of sight of the Earth's gravitational acceleration of the payload. The total change in radial velocity from the beginning to the end of the observing interval was 1.23 km s^{-1} for the target zenith angle of 66°.

A few picture elements immediately adjacent to the borders of the panels (and the timing signals) in Figure 2 were considered unreliable and thus were discarded. The gaps associated with the borders lose their identity in the composite picture (Fig. 3) because changes in rocket pointing caused them to shift relative to spectrum image coordinates. Mild irregularities in the image are evident at locations where the dwell time for a border was high, owing to possible time-dependent systematic errors and the greater relative noise caused by lower effective exposure times.

The composite exposures for positions 3 and 4 show three equidistant bright streaks running horizontally (coinciding with the panel borders). We believe that these streaks are caused by sporadic instabilities in the beginning and ending signal baselines within the frame-digitizing equipment. Spectral information in echelle orders adjacent to the streaks should be disregarded, or at least should be treated with great caution.

c) *Background Determinations and Extraction of Spectra*

Superposed on the spectrum was a smoothly changing background of photoevents produced by scattered light from the gratings and a diffuse Lyα background from the geocorona.

[1] The correspondence of motion is not exact. Strictly speaking, for a given translation of the reference image perpendicular to the echelle orders, the spectrum moves an additional one-fourth of this amount along the echelle orders. This mild cross-coupling of the x and y displacements is caused by changes in the cos σ term of the grating equation, where σ is the angle of the beam above and below the equator perpendicular to the echelle rulings ($\sigma = 3°.5$). Other than this effect, the motions of all parts of the spectrum and the reference image are coincident. (A correction for this cross-coupling was applied to translations of the *entire image*; since this correction is inappropriate for the reference images, they appear to be elongated in Fig. 3.)

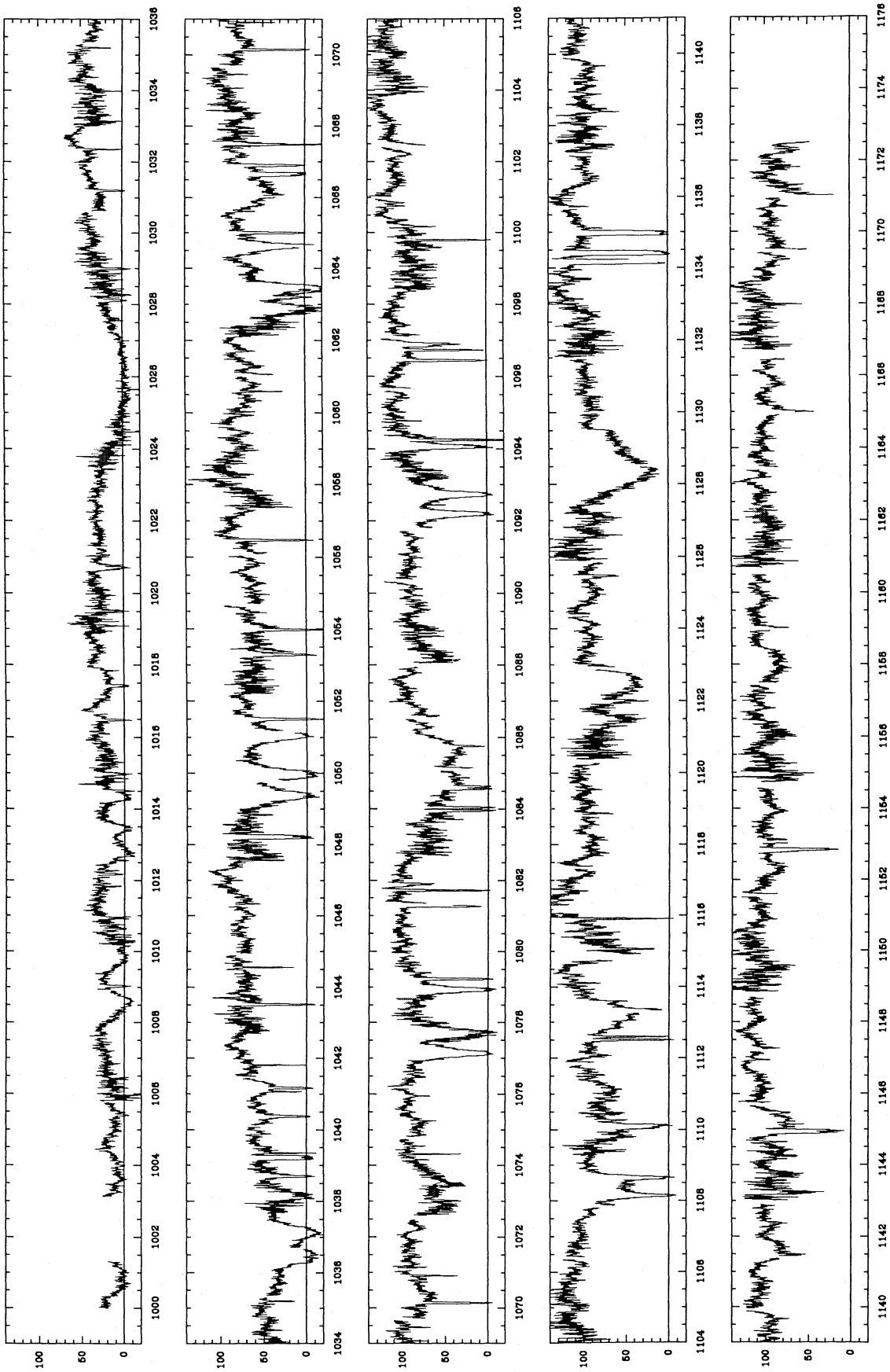

FIG. 4.—Spectrum of π Sco recorded by the Interstellar Medium Absorption Profile Spectrograph (IMAPS) on 1985 April 20. This tracing is a composite of all the echelle orders pieced together after a blaze ripple correction was applied to each of the four echelle tilt settings on each order. The periodic variability of noise in the continuum is caused by our sampling of some portions of the spectrum far from the optimum blaze angle.

The intensity of the background ranged from about 1 times the continuum level at the longest wavelengths to about twice the continuum at $\lambda \sim 1000$ Å. Background levels were evaluated from the mean interorder intensities on either side of a given order, after being convolved by a window function 60 pixels long with a smooth taper at each end. Corrections for some spillover of adjacent spectral orders into the interorder regions amounted to about 20% of the full intensity. The deep, saturated lines in Figure 4 indicate that the subtracted backgrounds were usually correct, but occasionally errors amounting to about 20% of the local continuum can be seen.

Spectra were extracted with a uniform slit function which had a height of 4 CCD pixels, a width of 1 pixel, and advanced $\frac{1}{2}$ pixel for each step along the spectrum. We had considered using a weighted, optimum sampling technique along the slit to increase the signal-to-noise ratio, in the manner described by Horne (1986). However, the crowding of adjacent orders prevented us from sampling very far into the wings of each order's vertical spread. As a consequence, we calculated that we could enhance the signal-to-noise ratio by only about 2.5%, even if the background counts were twice as large as the continuum. This small a gain did not seem to warrant the extra effort.

We believe that the principal source of vertical broadening of the echelle orders came from astigmatism, rather than a simple loss of focus or poor tracking of the rocket pointing. Evidence to support this notion comes from the slanted appearance of spectrum lines. Our extraction slit function in the analysis program had a matching inclination, so that we would not lose resolution.

Shear-type distortions in the image field mapping made the orders appear skewed near the edges of the frames. We invoked special corrections in the y motions of the sampling slit as it moved along the spectrum in x to compensate for this effect.

d) Wavelength Calibration

Before attempting to derive the fundamental parameters which governed the wavelength scale (e.g., reference locations on the image, image rotation angle, incidence and diffraction angles on each grating, etc.), we measured distortions in the image scale produced by irregularities in the magnetic and electrostatic fields in the image section of the detector. These measurements were performed after the flight with the detector in a laboratory vacuum tank. For this test, we installed a special photocathode which was prepared with the active CsI shadow-evaporated through a standard US Air Force Resolving Power Test Target lying on the substrate. A picture of this pattern was recorded by the detector when the photocathode was exposed to a uniform illumination from a UV lamp. For our study of image mapping, we compared actual locations of various sides of bars within the pattern to their respective apparent positions in the detector's output image. Over a vertical span equivalent to 40 echelle orders, the horizontal scale changed by 0.5%.

We used the wavelengths and measured positions of moderately strong H_2 absorption lines to define the free parameters in the grating equation. We calculated laboratory wavelengths of the H_2 transitions by subtracting the observed energy levels given by Dabrowski (1984). For each grating-tilt setting we could solve for all of the unknowns using the x-values for two lines, provided that they were reasonably different from each other. To minimize the possible influence of asymmetric profiles or velocity shifts from one J level to another, we attempted to work with lines from a single J that had similar strengths. The best collection of lines which satisfied this condition all came from the $J = 3$ level; however, we were forced to have one of the lines in position 1 arise from $J = 4$, since the only suitable $J = 3$ lines in the field had x-coordinates which were nearly the same. In retrospect, it seems that our precautions in choosing lines were not necessary, since there seems to be no coherent change in velocity across J levels or from weak to strong lines. H_2 lines which were actually used for deriving the wavelength scale are flagged in Tables 4 and 5 (see notes).

In addition to the H_2 lines, we were able to use very sharp lines from the three levels of fine structure of O I in the Earth's upper atmosphere. A narrow, weak line from telluric N I is also evident, just to the right of the strongest member of the triplet at 1135 Å (of interstellar origin). These atmospheric features, summarized in Table 2, not only served to check the derivations of relative scales using interstellar H_2 features but also provided an absolute velocity reference. We calculated that the Earth's rotation and orbital motion should shift the telluric lines to a heliocentric velocity of 16.49 km s^{-1}.

e) Wavelength Resolving Power

Since telluric lines are narrow, they represent the best choice for determining the velocity resolution of our spectrum. If we assume that the dimensions of the telluric O I profiles are the narrowest possible, i.e., perfectly box-shaped with widths equal to their equivalent widths, we find that the instrumental profile of IMAPS on this mission had a width of 2.4 km s^{-1} (FWHM). However, this figure is actually only a lower limit for our performance, for if the real telluric profiles had a slightly larger intrinsic width, one would conclude that our resolution was even better. The steepness of the edges of the interstellar N I lines confirms the resolving-power determination from the telluric lines.

f) General Features of the Spectrum

The rotational velocity of π Sco is rapid enough ($v \sin i = 100$ km s^{-1}) to smear out stellar features and create, at our resolution, a gently undulating continuum against which we can view the much sharper interstellar features. Most of the lines which are visible in Figure 4 are Lyman and Werner band transitions from various rotational levels of interstellar H_2 in its lowest vibrational state. So far, for H I regions we have identified features caused by such atoms and ions as C I, C II, N I, O I, P II, Cl I, Cl II, Fe II, and Ar I. There seem to be two distinct H II regions along the line of sight to π Sco, as evidenced by the double lines of N II near 1085 Å. Lines from S III and excited fine-structure levels of N II can be seen only for the region with the larger positive velocity, however. In accord

TABLE 2

TELLURIC ABSORPTION LINES

Absorber	λ (Å)	Echelle Position	Echelle Order	Heliocentric Velocity (km s^{-1})
O I*	1027.4307	1	220	15.6 ± 0.5
O I**	1028.1571	1	220	15.6 ± 0.5
O I	1039.2304	3	217	15.9 ± 0.3
O I*	1040.9425	2	217	17.1 ± 0.1
O I**	1041.6876	1	217	16.1 ± 0.1
N I	1134.9803	2	199	16.8 ± 0.3

NOTE.—O I wavelengths from Moore 1976; N I wavelengths from Moore 1975.

with previous findings from a survey by the *Copernicus* satellite, the line of sight toward π Sco has an unusually low column density of O VI; we cannot see any features at 1032 or 1037 Å. About 15 absorption features in the spectrum are yet to be identified.

IV. DATA ANALYSIS

a) Redeterminations of Backgrounds

As mentioned earlier (§ III*c*), background calculations which were made automatically by the extraction program were not consistently accurate. As we focused on the spectra near the H_2 lines, we found it necessary to refine the zero-intensity baselines before we undertook further analysis. Our preferred approach was to make the zero-intensity levels agree with the bottoms of well-resolved, saturated absorption lines (for either the line under question or some very nearby one). When this was not possible, we defined a zero such that the equivalent width W_λ of the H_2 line agreed with the curve of growth of lines from the same J level in the *Copernicus* observations of interstellar H_2 toward π Sco reported by Spitzer, Cochran, and Hirshfeld (1974). The precision of the backgrounds in *Copernicus* spectra was substantially better than that obtainable here.

The rms changes needed to redefine the zero levels from the originally created baselines equaled 0.16 times the local continuum for the different regions centered on the H_2 lines listed in Tables 3–6. Along with each new zero level, we estimated an uncertainty in the result. The rms uncertainties also turned out to be 16% of the respective continua. The most difficult background appraisals were for weak lines which were well isolated from other absorption features. For these lines, however, errors in the background were not of great importance.

Since the background determinations for some cases made use of information in the *Copernicus* data set, we must not overlook the fact that for some W_λ values, results from the two surveys are not genuinely independent. It is reassuring to note that for lines whose backgrounds were defined without reference to the results of Spitzer, Cochran, and Hirshfeld (1974), our results were in satisfactory agreement with theirs.

b) Measurements of H_2 Lines

For each H_2 absorption line, we defined a continuum by fitting a low-order polynomial to the nearby intensities which were not obviously affected by an absorption line (except when the line being measured and neighboring intensities were all on a shallow wing of an adjacent, broad line). We then measured the first 3 moments of the absorption feature (i.e., cW_λ/λ, the velocity centroid $\bar{v}$, and the line's second moment $\langle v - \bar{v} \rangle^2$). Results for rotational excitations $J = 2$ to $J = 5$ are given in Tables 3–6. Figure 5 shows a sampling of profiles from each of the J levels. These examples are representative of cases with relatively good signal quality (cf. error estimates in the tables).

The H_2 transitions listed in the tables are ranked according to their respective values of $\log f\lambda$, taken from Morton and Dinerstein (1976). The oscillator strengths listed in that paper are from Allison and Dalgarno (1970) and have been corrected wherever possible for nonadiabatic effects according to Ford (1975). Unfortunately, no such correction factors are available for the $R(5)$ lines, so that the oscillator strengths for these lines may be somewhat in error. However, since the observed Lyman lines in this work involve upper levels $v' < 10$, the uncertainties are expected to be at most 20%.

We computed errors in the three profile moments using the formulae in the appendix of Bohlin *et al.* (1983)[2] and combining the results in quadrature with the calculated values for errors caused by baseline uncertainties. In each case, we evaluated the local random noise level by measuring fluctuations of the intensities about the defined continuum. We assumed a

[2] The formulae account for errors from noise in the recorded intensities, together with the lowest order of uncertainty in the position of a continuum. Errors in the *exact shape* of the continuum are not calculated, however.

TABLE 3

H_2 LINES FROM $J = 2$

Transition	λ (Å)	$\log f\lambda$	Echelle Position	Echelle Order	cW_λ/λ (km s^{-1})	$\bar{v}$ (km s^{-1})	$\langle v - \bar{v} \rangle^2$ (km^2 s^{-2})	m.a.d. (km s^{-1})
Lyman 0–0 $P(2)$[a]	1112.496	−0.131	2	203	12.07 ± 0.60	−17.43 ± 0.13	15.7 ± 0.7	5.38 ± 0.34
Lyman 1–0 $P(2)$	1096.438	0.398	2	206	14.13 ± 0.64	−17.27 ± 0.11	20.0 ± 0.5	6.38 ± 0.35
Lyman 1–0 $R(2)$	1094.245	0.604	3	206	14.60 ± 2.01	−15.79 ± 0.22[b]	19.3 ± 0.9	6.46 ± 0.74
Lyman 1–0 $R(2)$	1094.245	0.604	4	206	13.63 ± 1.19	−18.57 ± 0.18[b]	20.9 ± 0.9	6.36 ± 0.56
Lyman 2–0 $P(2)$[c]	1081.265	0.690	2	209	14.91 ± 0.60	−17.72 ± 0.08[b]	22.7 ± 0.4	6.91 ± 0.25
Werner 0–0 $P(2)$	1012.169	0.730	2	223	15.42 ± 2.16	−17.78 ± 0.25[b]	18.8 ± 1.2	6.29 ± 0.74
Lyman 3–0 $P(2)$	1066.900	0.865	1	212	16.56 ± 0.73	−19.15 ± 0.13	29.1 ± 0.6	7.78 ± 0.40
Lyman 2–0 $R(2)$	1079.225	0.902	3	209	14.78 ± 0.69	−18.34 ± 0.15	22.1 ± 0.7	6.89 ± 0.47
Lyman 4–0 $P(2)$	1053.284	0.966	4	214	17.39 ± 1.40	−18.48 ± 0.24[b]	31.7 ± 1.3	8.05 ± 0.78
Lyman 8–0 $P(2)$[d]	1005.392	0.993	1	225	14.74 ± 2.24	−16.38 ± 0.40	22.1 ± 1.8	6.80 ± 1.32
Lyman 7–0 $P(2)$	1016.461	1.011	3	222	14.84 ± 1.78	−16.96 ± 0.20	23.6 ± 0.9	6.65 ± 0.68
Lyman 5–0 $P(2)$	1040.367	1.016	2	217	15.68 ± 1.20	−16.89 ± 0.30	24.8 ± 1.5	7.29 ± 0.91
Lyman 6–0 $P(2)$[e]	1028.105	1.029	1	220	19.02 ± 1.52	−18.77 ± 0.32	41.9 ± 1.9	9.04 ± 1.19
Lyman 3–0 $R(2)$	1064.995	1.080	2	212	17.28 ± 0.69	−16.96 ± 0.17	29.3 ± 1.0	7.98 ± 0.51
Lyman 4–0 $R(2)$	1051.498	1.189	1	215	17.56 ± 1.26	−17.84 ± 0.25	32.8 ± 1.7	8.04 ± 0.69
Werner 0–0 $R(2)$	1009.024	1.221	1	224	19.27 ± 1.94	−19.08 ± 0.29	32.2 ± 1.6	8.34 ± 0.89
Lyman 5–0 $R(2)$	1038.690	1.247	4	217	16.22 ± 2.46	−16.80 ± 0.51	20.6 ± 3.3	7.39 ± 1.42

[a] Possible interference from C I* at 1112.472 Å (however, a line in the same multiplet from C I λ1112.269 seems not to be evident).
[b] Line is located near the edge of the frame, hence its velocity may not be reliable.
[c] No continuum on the right-hand side (cut off by the edge of the frame).
[d] Recording of this profile is significantly inferior to others with comparable values of $\log f\lambda$. Omitted from Figs. 6 and 8.
[e] Possible interference from O I* at 1028.145 Å and/or O I** at 1028.157 Å ($f = 0.02$; this value is higher than those of O I** lines in other multiplets).

TABLE 4

H_2 LINES FROM $J = 3$

Transition	λ (Å)	$\log f\lambda$	Echelle Position	Echelle Order	cW_λ/λ (km s^{-1})	$\bar{v}$ (km s^{-1})	$\langle v - \bar{v}\rangle^2$ (km^2 s^{-2})	m.a.d. (km s^{-1})
Lyman 0–0 $P(3)$[a]	1115.896	−0.105	3	202	4.96 ± 1.29	−12.89 ± 0.72[b]	9.5 ± 3.2	3.39 ± 1.96
Lyman 0–0 $P(3)$	1115.896	−0.105	4	202	6.86 ± 0.95	−16.87 ± 0.24[b]	11.1 ± 0.8	4.10 ± 0.66
Lyman 0–0 $R(3)$	1112.584	0.055	2	203	8.63 ± 0.40	−17.19 ± 0.11	12.2 ± 0.4	4.31 ± 0.29
Lyman 1–0 $P(3)$[c]	1099.787	0.422	3	205	10.19 ± 1.05	−15.82 ± 0.18	10.8 ± 0.6	4.46 ± 0.61
Lyman 1–0 $R(3)$[c]	1096.725	0.589	2	206	10.39 ± 0.43	−17.60 ± 0.09	13.9 ± 0.4	4.86 ± 0.28
Lyman 3–0 $P(3)$[c, d]	1070.141	0.887	2	211	12.88 ± 0.71	−16.92 ± 0.11	16.7 ± 0.4	5.79 ± 0.35
Lyman 2–0 $R(3)$[c]	1081.711	0.887	1	209	12.93 ± 0.57	−16.99 ± 0.13	18.9 ± 0.7	5.81 ± 0.35
Werner 0–0 $P(3)$[e]	1014.504	0.899	1	223	14.14 ± 2.79	−17.62 ± 0.39	20.0 ± 1.6	6.26 ± 1.36
Lyman 4–0 $P(3)$	1056.471	0.987	1	214	13.46 ± 0.93	−18.06 ± 0.16	17.6 ± 0.7	5.89 ± 0.54
Lyman 5–0 $P(3)$[c, f]	1043.503	1.036	4	216	15.09 ± 1.40	−17.05 ± 0.16	23.9 ± 0.7	6.83 ± 0.47
Lyman 6–0 $P(3)$	1031.192	1.047	2	219	13.04 ± 1.13	−18.09 ± 0.31	17.7 ± 1.7	5.91 ± 0.91
Lyman 3–0 $R(3)$[c, g]	1067.478	1.066	4	211	10.80 ± 2.43	−16.62 ± 0.51	14.7 ± 2.2	4.66 ± 1.61
Werner 0–0 $R(3)$[g]	1010.130	1.172	1	224	13.91 ± 5.87	−15.44 ± 1.12[b]	23.4 ± 6.7	6.71 ± 2.35
Lyman 4–0 $R(3)$[c]	1053.976	1.175	3	214	13.91 ± 1.46	−17.11 ± 0.32	21.4 ± 1.6	6.36 ± 0.93
Lyman 9–0 $R(3)$[g]	995.972	1.205	1	227	12.28 ± 8.40	−18.74 ± 1.60[h]	13.3 ± 6.4	6.16 ± 5.90
Lyman 5–0 $R(3)$	1041.158	1.232	2	217	14.47 ± 0.67	−16.61 ± 0.14	19.3 ± 0.6	6.55 ± 0.44
Lyman 6–0 $R(3)$[g, i]	1028.986	1.260	4	219	14.79 ± 2.52	−16.49 ± 0.47	21.5 ± 2.0	6.56 ± 1.61
Lyman 7–0 $R(3)$[j]	1017.424	1.272	2	222	$\gtrsim$16.50	...	...	...

[a] Profile very close to the left-hand edge of the frame; only the right-hand edge of the profile was included in Figs. 6 and 8.
[b] Line is located near the edge of the frame, hence its velocity may not be reliable.
[c] Line was used in the determination of the velocity scale (see § III*d*).
[d] Possible interference from Fe II at 1070.135 Å (but the line should be well inside the H_2 profile).
[e] In the broad wing of the Lyman 7–0 $P(1)$ profile, but the modified continuum is well defined.
[f] Possible interference from Fe II at 1043.486 Å.
[g] Recording of this profile is significantly inferior to others with comparable values of $\log f\lambda$. Omitted from Figs. 6 and 8.
[h] This velocity omitted from the average, since the error given here is significantly larger than the dispersion of the other velocities.
[i] May be contaminated by telluric O I at 1028.870 Å.
[j] Interference from the Werner 0–0 $P(4)$ line on the far left-hand side; hence the profile is not complete.

TABLE 5

H_2 LINES FROM $J = 4$

Transition	λ (Å)	$\log f\lambda$	Echelle Position	Echelle Order	cW_λ/λ (km s^{-1})	$\bar{v}$ (km s^{-1})	$\langle v - \bar{v}\rangle^2$ (km^2 s^{-2})	m.a.d. (km s^{-1})
Lyman 1–0 $P(4)$[a]	1104.084	0.432	4	204	2.58 ± 0.85	−16.41 ± 0.81	14.0 ± 2.9	5.06 ± 2.08
Lyman 1–0 $R(4)$	1100.164	0.582	3	205	3.00 ± 0.51	−16.32 ± 0.47	9.3 ± 1.5	3.66 ± 1.61
Lyman 2–0 $P(4)$	1088.795	0.724	4	207	3.63 ± 0.61	−17.46 ± 0.36	9.3 ± 1.3	3.76 ± 1.08
Lyman 2–0 $R(4)$	1085.145	0.881	2	208	5.53 ± 1.16	−15.55 ± 0.29[b]	10.0 ± 1.1	4.10 ± 1.01
Lyman 3–0 $P(4)$	1074.313	0.896	3	210	4.13 ± 0.36	−17.91 ± 0.19	7.0 ± 0.8	3.12 ± 0.37
Werner 0–0 $P(4)$[a, c]	1017.385	0.971	2	222	5.01 ± 2.01	−16.83 ± 0.81	4.1 ± 3.7	1.92 ± 1.94
Lyman 4–0 $P(4)$	1060.581	0.994	2	213	4.48 ± 0.41	−17.51 ± 0.21	9.3 ± 0.7	3.62 ± 0.86
Lyman 7–0 $P(4)$[a]	1023.436	1.014	1	221	5.64 ± 1.32	−18.44 ± 0.41	10.9 ± 1.3	3.99 ± 1.08
Lyman 8–0 $P(4)$[a]	1012.262	1.022	2	223	7.08 ± 2.03	−17.52 ± 0.29	12.6 ± 0.9	4.67 ± 1.09
Lyman 5–0 $P(4)$[d]	1047.552	1.041	1	216	5.06 ± 0.45	−17.19 ± 0.20[b]	8.4 ± 0.7	3.30 ± 0.63
Lyman 6–0 $P(4)$	1035.182	1.048	3	218	5.44 ± 0.95	−15.97 ± 0.19[b]	7.6 ± 0.6	3.36 ± 0.71
Lyman 3–0 $R(4)$	1070.900	1.059	2	211	4.14 ± 0.28	−17.23 ± 0.14[b]	7.6 ± 0.4	3.14 ± 0.44
Lyman 4–0 $R(4)$	1057.380	1.170	1	214	6.32 ± 0.71	−17.33 ± 0.21[b]	10.7 ± 0.7	3.83 ± 0.56
Werner 0–0 $R(4)$[a]	1011.814	1.181	3	223	6.36 ± 1.71	−15.76 ± 0.54	5.4 ± 3.1	3.47 ± 1.30
Lyman 5–0 $R(4)$	1044.543	1.228	3	216	5.86 ± 0.57	−16.80 ± 0.15	7.4 ± 0.5	3.27 ± 0.48
Lyman 6–0 $R(4)$	1032.350	1.257	1	219	6.83 ± 1.01	−18.54 ± 0.29	10.5 ± 1.0	3.68 ± 1.02
Lyman 7–0 $R(4)$[e]	1020.767	1.267	3	221	5.34 ± 0.94	−17.44 ± 0.31	3.5 ± 1.2	2.66 ± 0.81

[a] Recording of this profile is significantly inferior to others with comparable values of $\log f\lambda$. Omitted from Figs. 6 and 8.
[b] Line is located near the edge of the frame, hence its velocity may not be reliable.
[c] Located in the wing of the Lyman 7–0 $R(3)$ absorption, hence not reliable.
[d] Line was used in the determination of the velocity scale (see § III*d*).
[e] Continuum hard to define on the left-hand side due to the presence of Fe II at 1020.722 Å and Si II at 1020.699 Å. Omitted from Figs. 6 and 8.

TABLE 6

H_2 LINES FROM $J = 5$

Transition	λ (Å)	$\log f\lambda$	Echelle Position	Echelle Order	cW_λ/λ (km s^{-1})	$\bar{v}$ (km s^{-1})	$\langle v - \bar{v}\rangle^2$ (km^2 s^{-2})	m.a.d. (km s^{-1})
Lyman 1–0 $R(5)$[a]	1104.548	0.537	4	204	-0.08 ± 0.39	...	...	...
Lyman 2–0 $P(5)$[a, b]	1093.955	0.729	4	206	0.79 ± 0.39	-18.03 ± 0.80	1.0 ± 1.6	1.47 ± 2.28
Lyman 2–0 $R(5)$[a]	1089.513	0.832	3	207	-0.16 ± 0.32	...	...	...
Lyman 3–0 $P(5)$[a]	1079.400	0.900	3	209	1.66 ± 0.32	-17.88 ± 0.37	5.6 ± 0.7	3.19 ± 3.23
Lyman 4–0 $P(5)$	1065.596	0.997	2	212	1.54 ± 0.29	-16.84 ± 0.38	5.2 ± 0.8	2.78 ± 1.01
Lyman 3–0 $R(5)$	1075.244	1.008	2	210	1.16 ± 0.29	-16.82 ± 0.47	3.0 ± 0.9	1.90 ± 1.71
Lyman 7–0 $P(5)$[c, d]	1028.248	1.011	1	220	1.42 ± 0.59	-18.52 ± 0.69	5.9 ± 1.5	2.81 ± 2.34
Lyman 8–0 $P(5)$[c]	1017.004	1.037	2	222	1.09 ± 0.74	-15.49 ± 1.86[e]	5.5 ± 6.0	1.70 ± 2.13
Lyman 5–0 $P(5)$	1052.497	1.043	1	215	0.93 ± 0.22	-17.04 ± 0.39[f]	0.4 ± 1.1	1.09 ± 0.93
Lyman 6–0 $P(5)$	1040.059	1.046	3	217	1.16 ± 0.23	-17.27 ± 0.29[f]	3.1 ± 0.9	2.16 ± 0.89
Lyman 4–0 $R(5)$[g]	1061.697	1.109	1	213	1.88 ± 0.31	-17.01 ± 0.47	7.7 ± 1.6	3.53 ± 1.41
Lyman 5–0 $R(5)$	1048.831	1.164	3	215	2.53 ± 0.52	-16.94 ± 0.34	6.3 ± 0.7	3.06 ± 1.01
Werner 0–0 $Q(5)$	1017.831	1.381	2	222	3.88 ± 0.68	-16.26 ± 0.34[f]	5.2 ± 1.1	2.58 ± 0.74

[a] Absorption is too weak to give reliable profile imformation. Not included in Figs. 6 or 8.
[b] Possible interference from Fe II at 1093.954 Å.
[c] Recording of this profile is significantly inferior to others with comparable values of $\log f\lambda$. Omitted from Figs. 6 and 8.
[d] Right-hand continuum has a strong line: telluric O I** at 1028.157 Å. Also, absorption by telluric O I* at 1028.145 Å may be a problem.
[e] This velocity omitted from the average, since the error given here is significantly larger than the dispersion of the other velocities.
[f] Line is located near the edge of the frame, hence its velocity may not be reliable.
[g] Probable interference from Fe II at 1061.684 Å. A semiempirical f-value from Kurucz and Peytremann 1975 is 2.5×10^{-5}, so the line could have a strength $\gtrsim 0.0007$ times as great as the absorption we see at 1096.886 Å (see Fig. 4). While this H_2 profile appears to be of good quality, it is not included in Figs. 6 and 8.

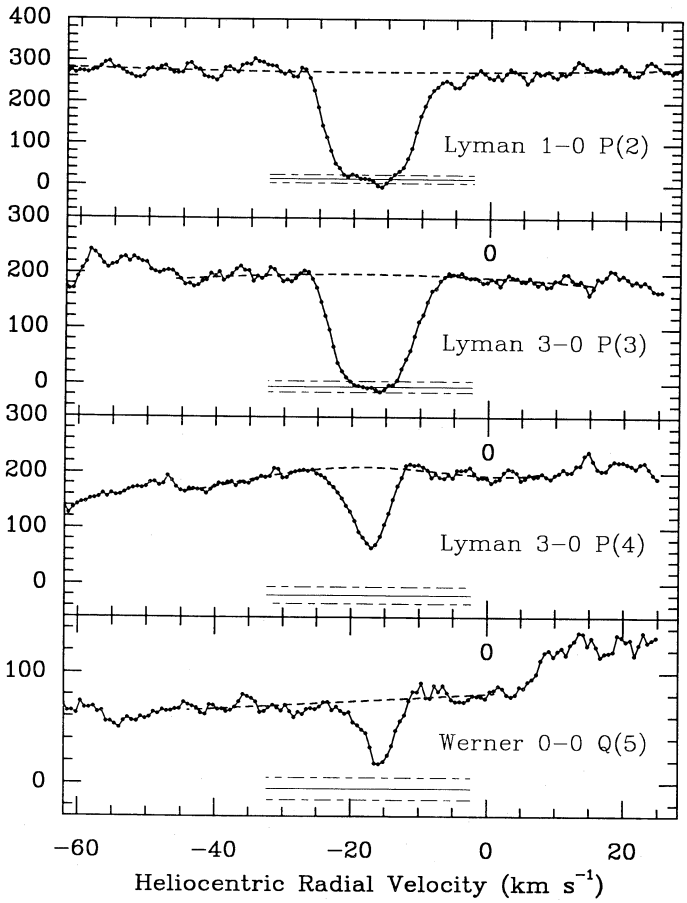

FIG. 5.—Samples of intensity plots for H_2 absorption lines from 4 different J levels. The sample points are spaced $\frac{1}{2}$ CCD pixel apart. In each case we show the assumed levels for the continuum (*dashed lines*) and redefined zero baseline (straight, solid line flanked by dashed lines showing the adopted error estimates for the zero levels; see § IV*a*).

coherence length for the noise fluctuations equal to the width of 1.5 CCD pixels (i.e., 1.9 km s^{-1}).[3] For lines with good signal-to-noise ratios, errors in the velocity centroids are governed primarily by high-order distortions in the image scale which were not corrected. Likewise, errors in the second moments are probably dominated by uncertainties in continuum curvature or the presence of inconspicuous absorption features. These effects are not included in the formal errors listed in the tables. One should also note some special warnings stated by Bohlin *et al.* about the reliability of even the formal error figures. Thus, probably the most reliable assessment of errors for $\bar{v}$ and $\langle v - \bar{v}\rangle^2$ would be an analysis of the variance in the results for groups of lines near each other in the tables. The formal errors should serve as a guide on the importance of noise processes and how they differ from one case to another.

An alternative, more robust method of measuring the width of an absorption profile is to calculate the median absolute deviation (m.a.d.) away from the profile's median velocity (Mosteller and Tukey 1977). Measured values of the m.a.d. and their estimated errors are given in the last columns of the tables.

While many H_2 features from $J = 0$ and $J = 1$ were observed, the profiles were so broad that it was difficult for us to improve on the results of Savage *et al.* (1977), who derived column densities for H_2 in the lowest two rotational levels by finding the best correspondence between the profiles recorded by *Copernicus* and theoretical ones for different $N(H_2)$. Because of uncertainties in baselines (see § III*c*) and continua over the relatively large wavelength intervals, we report here only the measurements of $\bar{v}$, so that they can be compared with those we

[3] An analysis performed later showed that this assumed value for the coherence length of errors was too large; a length of 1 CCD pixel seems more correct. Hence the true errors shown in Tables 2–7 are slightly smaller than those listed. The benefits from retroactively recomputing the errors did not seem large enough to justify the substantial effort required. The appraisal of the errors listed in Table 8 (see § IV*f*) assumed that statistically independent readings were 1 CCD pixel apart.

obtained for higher J. The entries in Table 7 show that the errors in $\bar{v}$ for $J < 2$ are relatively large.

c) *Velocity Centroids for Different J*

Values of $\bar{v}$ listed in Tables 3–6 seem not to show any steady trends as the lines become stronger, even though the profiles are slightly asymmetric (see Figs. 6 and 8). Hence the standard errors $s_{\bar{v}}$ are a reasonable measure of the true errors in our line-position measurements. Table 7 displays the straight averages of $\bar{v}$ for each J level. We felt that it was inappropriate to use a weighted average, with weights proportional to the inverse squares of the formal (noise-related) errors, since the latter were generally much smaller than the standard errors of the samples. (Only two lines listed in the tables had formal errors which were significantly larger than $s_{\bar{v}}$, and these cases were not included in the averages.) Errors given for $\bar{v}$ are simply $n^{-1/2}s_{\bar{v}}$, where n is the number of $\bar{v}$ entries considered in the average.

The results in Table 7 indicate that we cannot see any convincing difference in the radial velocity of H_2 from one J level to the next. This conclusion provides a constraint for interpretations which might invoke an interstellar shock as a source of rotational excitation, provided that the shock is not moving transversely to the line of sight.

d) *Profile Shapes*

There are two important qualities in our observations of H_2 toward π Sco by IMAPS which make it appealing to study the structures of the velocity profiles. First, the instrumental profile is distinctly narrower than even the unsaturated H_2 lines (with the possible exception of the lines from $J = 5$). For instance, the m.a.d. for the weaker telluric absorption features (e.g., those of O I**) is of order 1.5 km s^{-1}, compared with 3.4 km s^{-1} (a weighted average) for the entries in the top half of Table 5. This difference gives us at least a superficial indication that we have resolved the velocity structure (but see a later discussion of this issue). The second important property of our spectrum is that many absorption lines of different strength were recorded from individual J levels. Lines shown in the tables have $\log f\lambda$ values which span about 1 order of magnitude. This selection allows us to consider a very generous range in $N(H_2)$ per unit velocity without our having to interpret portions of the profile which are either badly saturated or buried in the noise. For our best example, $J = 3$, our composite result spans a factor of 100 over different parts of the column density profile.

If we assume that the profiles are perfectly resolved by the instrument, we can convert the recorded intensities I into optical depths $\tau = -\ln(I/I_{cont})$ as a function of velocity. In the four panels of Figure 6 we have plotted the optical depths for different lines on a logarithmic scale for J levels 2–5. These plots depict only parts of the profile where $0.10 < I/I_{cont} < 0.90$, except for $J = 5$, where we permitted absorptions as small as $I/I_{cont} = 0.975$ to be shown. In every case, we added 14.576 and subtracted a transition's $\log f\lambda$ to convert $\log \tau$ to a scale representing $\log N(H_2)$ per unit velocity interval.

Each profile was shifted horizontally in the plot by a small amount, so that its median intensity was at a velocity of -17.44 km s^{-1}. This adjustment, never more than about 2 km s^{-1}, was designed to reduce the changing velocity offsets caused by the uncorrected systematic errors in our wavelength scale (see § III*d*). In principle, there may be ways in which this procedure could give some misleading general conclusions, since information in the profile itself is used to govern the magnitude and direction of the correction. However, it is reassuring to note that the dispersions of the velocity corrections do not vary significantly from one J level to another: for the profiles exhibited in Figures 6*a*–6*d* the rms shifts were 0.94, 0.66, 0.76, and 0.58 km s^{-1}, respectively.

At first sight, the nearly parabolic shapes of the profiles seem to indicate that the H_2 molecules have projected velocity distributions which are close to being Gaussian (see § IV*f*). Indeed, the widths of the distributions are approximately consistent with the b-value of 3.8 km s^{-1} derived by Spitzer, Cochran, and Hirshfeld (1974) from their composite (standard) curve of growth for several J levels. This simple interpretation seems to be flawed, however. For $J = 2$ and $J = 3$ the inner portions of the profiles from strong transitions (shown by the boldest markers in the figure) seem to contradict the determinations, at the same velocities, for the amount of $N(H_2)$ per unit velocity from the much weaker transitions (i.e., the profiles delineated by small dots). This effect seems to be absent for $J = 4$ and $J = 5$, presumably because the absorptions are never very strongly saturated.

It is tempting to think that the differences in the rescaled optical depths on the sides of the strong and weak absorption features could be caused by the appearance of damping wings. The effect works in the right sense, since the upper levels for stronger lines have generally longer lifetimes than those for the weaker transitions that we observed. However, the magnitude of the difference is not correct. At any particular velocity displacement from the line's core, the effective τ is proportional to $\lambda^2\gamma f$. If damping wings were the *only source* of opacity, vertical

TABLE 7

AVERAGES OF VELOCITY CENTROIDS FOR ABSORPTION PROFILES

J	Average Heliocentric $\bar{v}$ (km s^{-1})	$s_{\bar{v}}$ (km s^{-1})	Lines Considered in Average
0.....	-17.3 ± 1.8	3.6	Lyman 0–0, 1–0, 2–0, and 4–0 $R(0)$
1.....	-18.4 ± 1.2	2.1	Lyman 0–0 $R(1)$, 1–0 $R(1)$, and 2–0 $P(1)$
2.....	-17.66 ± 0.28	0.96	All entries in Table 3 except those identified with note b
3.....	$-17.09 + 0.18$	0.64	All entries in Table 4 except those identified with notes b and h
4.....	-17.24 ± 0.25	0.85	All entries in Table 5 except those identified with note b
5.....	-17.43 ± 0.26	0.69	All entries in Table 6 except those identified with notes e and f

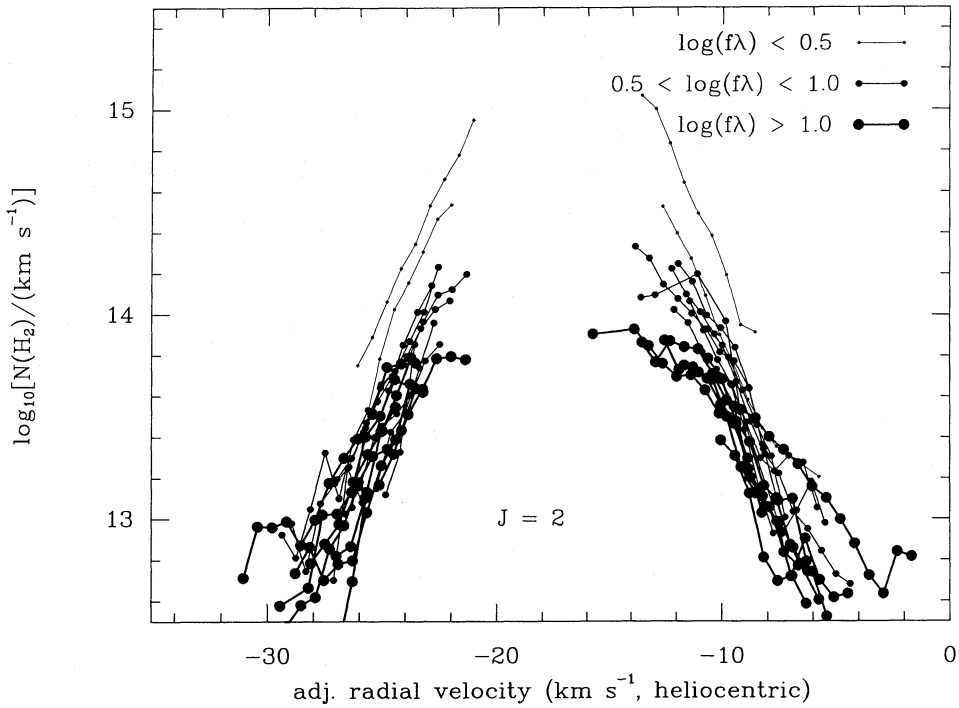

FIG. 6*a*

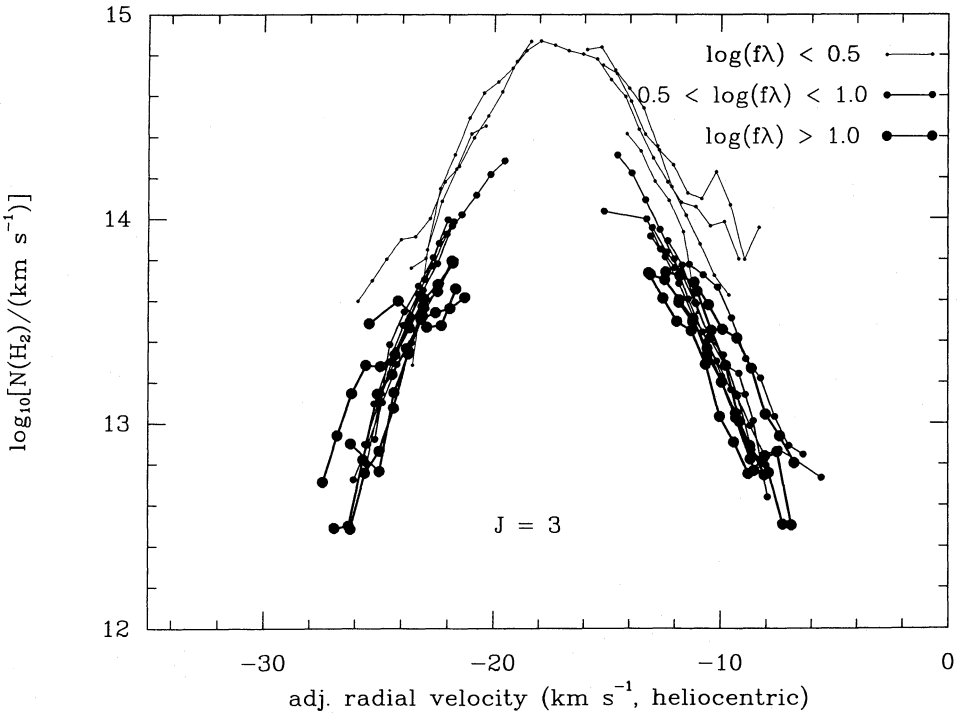

FIG. 6*b*

FIG. 6.—Superposition of velocity profiles of H_2 in the lowest vibrational state with rotational quantum numbers J ranging from 2 to 5 (*a–d*), derived from the *R* and *P* branch members of Lyman (and a few Werner) transitions listed in Tables 3–5 with different vibrational quantum numbers v' for the upper electronic state. These curves were derived by converting relative intensities above background into optical depths, assuming that the curves were perfectly resolved. (The disparity between strong and weak lines for $J = 2$ and $J = 3$ shows that this assumption is incorrect, however; see § IV*e*). Before they were plotted, the curves were translated vertically by an amount $14.576 - \log f\lambda$ to convert $\log \tau$ to $\log N(H_2)$ per unit velocity interval.

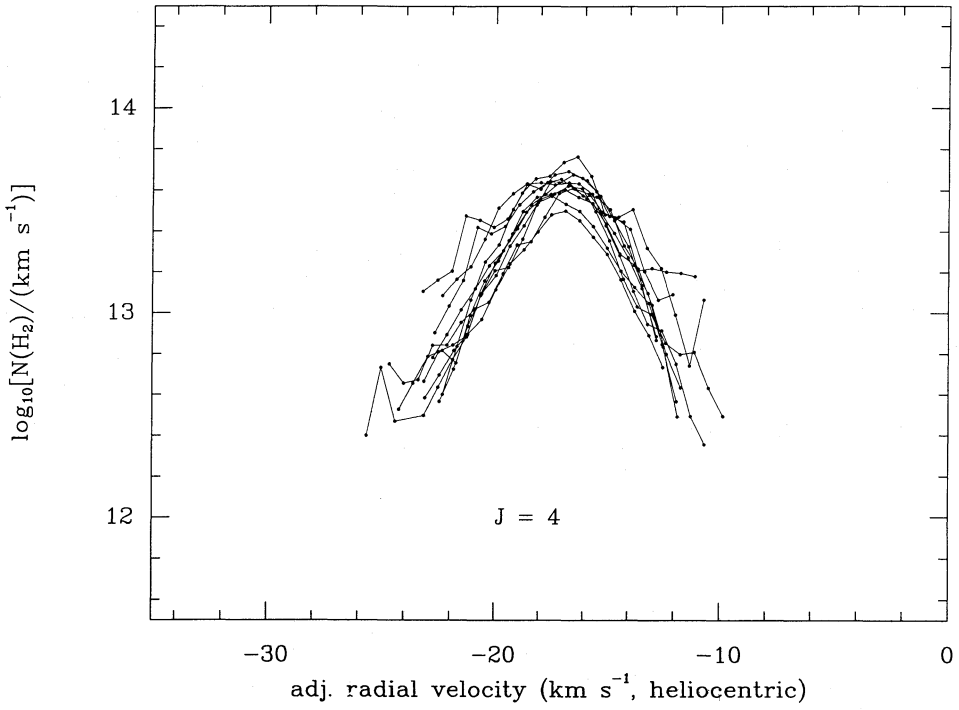

FIG. 6c

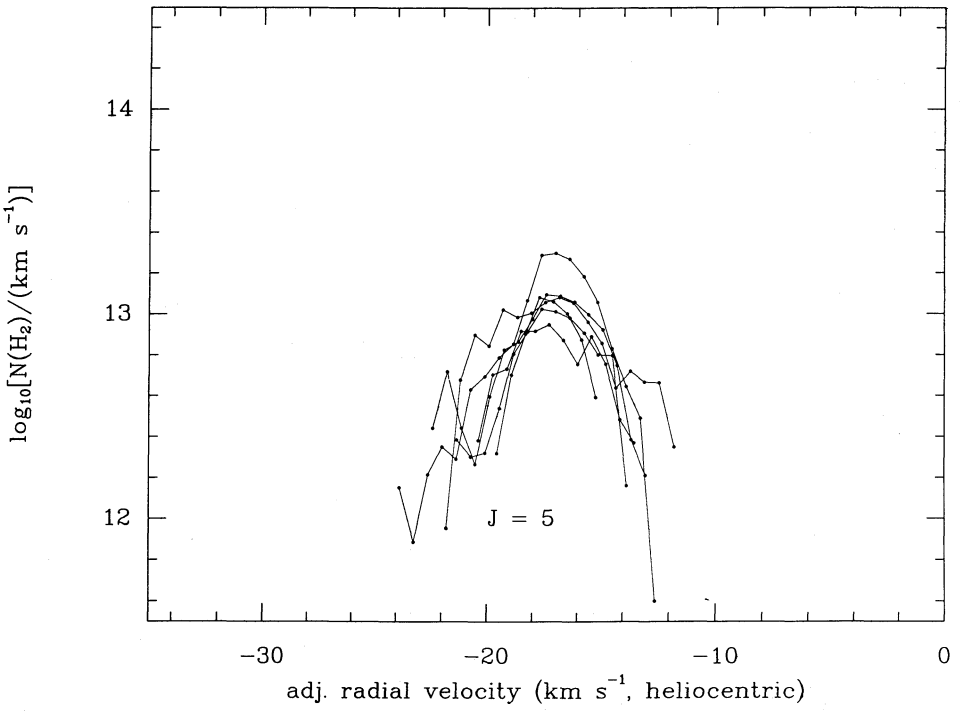

FIG. 6d

displacements in the plots would equal changes ~ 0.2 in log $\lambda\gamma$ from the strong to weak lines, a value considerably less than the perceived differences in log $\tau/f\lambda$.

In principle, we could explain the persistent disparity between strong and weak lines if the estimated background baselines were consistently lower than the real levels of zero intensity in the spectrum. For our data, however, this interpretation will not work. We would need to raise the background well above a profile's observed central intensity in order to make the inferred optical depth on the sides increase by the amount required to resolve the discrepancy.

A more elaborate explanation of the problem might be to propose that the IMAPS instrumental profile consisted of the principal, narrow spike on top of a broad shoulder caused by small-angle scattering of light by the echelle grating. The effect of this extra scattering contribution in most places would be to

raise the overall background, but there would be no noticeable effect on wavelength resolution. If the characteristic width of the shoulder were wider than the weak H_2 lines but not the strongly saturated ones, there would be an anomalous depression of the generally high background level immediately near the core of a strong line. If we used the observed intensity at the bottom of the line to define a background and then assumed that the level somewhat removed from this core was unchanged, we would underestimate the optical depth along the edges of the line. This error, in effect, could produce the strange behavior we see in Figures 6*a* and 6*b*. Fortunately, this perverse instrumental problem does not seem to apply to our observation of π Sco. The sharp, boxy appearance of the interstellar N I lines at 1134–1135 Å assures us that there is no scattering component whose width would be about right to make this particular process work. While the H_2 lines in our study occur at shorter wavelengths, we do not expect an appreciable increase in scattered light, since the intensity either should be independent of the grating order m or should scale with m^2, depending on the source of such scattering (Meyer 1949).

There is an alternative to the viewpoint that our backgrounds are in error. We can propose that our spectrum is not really resolving the finest details in the structures of the profiles. Indeed, we believe this is the most plausible explanation of our problem. Suppose that, instead of the regularly shaped profiles depicted in Figure 6, we had real velocity profiles which consisted of tight clusters of very narrow spikes not resolved individually by IMAPS. If the intensity contrast between the peaks and valleys of these unresolved features were large, our optical depth plots would not correctly represent the smoothed optical depths. For the transitions with low f-values, however, optical depths would be approximately correct because the logarithmic conversion from relative intensity levels of weak absorptions would be nearly linear.

e) A Model for Fine Structure

To show that the above explanation based on unresolved velocity structure is reasonable, we constructed a hypothetical model of a complex profile and demonstrated that our instrumental smoothing could produce the observed behavior for the strong and weak $J = 2$ and $J = 3$ lines of H_2. To create the roughly parabolic shape for the observed smoothed profiles, we constructed a symmetrical array of seven narrow components, each of differing amplitude, clustered in a manner resembling fingers on a hand. Strictly speaking, the model proves only the existence of an explanation for the profiles we recorded. While we could not defend the uniqueness of this model in a rigorous manner, we nevertheless found that it was difficult to propose variants without violating some aspect of the observed profiles.

The misrepresentation of optical depths after smoothing should obviously become worse as the velocity dispersions b of the fingers decrease. However, it is not physically realistic to have their characteristic b smaller than the thermal Doppler broadening for the gas's temperature. By comparing the column densities of H_2 in the $J = 0$ and $J = 1$ states, Savage *et al.* (1977) derived a rotation temperature of 81 K. This rotation temperature is strongly coupled to the kinetic temperature through exchange reactions with free protons which convert ortho-hydrogen to para-hydrogen and vice versa (Dalgarno, Black, and Weisheit 1973). As a start, we adopted a b-value of 0.82 km s^{-1} for each finger, a dispersion which corresponds to the 81 K temperature. We discovered that we could not reproduce the magnitude of the disparity between strong and weak lines near the wings of the profile if the b were uniformly this large, however. Thus, for some of the H_2 toward π Sco, in particular the components with the largest velocity displacements from the core of the complex, we needed to lower the assumed velocity dispersions (and temperatures). To compensate for this change and maintain the proper overall ortho to para ratios, we raised the temperatures of the middle three components.

After some experimentation, we arrived at the following relative positions and column densities for the seven components in the $J = 3$ state. The strongest component had 39% of the material, and it was located at the center of the complex. This principal feature was flanked on both sides by three other components: one component at 2.5 km s^{-1} with a 26% portion of the total, another at a distance of 5 km s^{-1} with 4.2%, and finally a component at 7.5 km s^{-1} contributing only 0.6%. The middle three components had $b = 0.91$ km s^{-1}—a Doppler spread equivalent to having $T = 100$ K, while the b-value for the four outermost profiles was set to 0.70 km s^{-1} ($T = 60$ K).

Figure 7 exhibits a simulation of the analysis used to produce plots of the character shown in Figure 6, but with the model array of profiles instead of real data. The dashed line shows the result we would have obtained if our resolution were as good as $\frac{1}{2}$ CCD pixel (0.625 km s^{-1}), while the topmost solid line shows the result of solving for $\tau(v)$ using intensities which have been convolved with a Gaussian function having a FWHM = 2.4 km s^{-1} (from § III*e*). Recalling that the presentation is logarithmic, we can see that this solid line depicts with reasonable accuracy a smoothed version of the original profile. Up to this point, we are working with a group of lines which is not very strong (largest $\tau_0 = 1.0$).

We now repeat the analysis of smoothed data, but with an ensemble whose τ's are uniformly stronger by a factor of $10^{0.5}$, thus simulating what we would obtain with a molecular line having a larger transition probability. This result is again plotted in Figure 7, but with a downward vertical offset of 0.5 which duplicates our $-\log f\lambda$ corrections in Figure 6. This new curve now falls slightly below the first curve. It would have fallen on top of the curve for the weaker line were it not for the error caused by our deriving $\tau(v)$ in a simpleminded fashion for partly saturated components whose intensities have been smoothed. In accord with our qualitative expectation in this study, we can see that now the average optical depths are underestimated. The behavior for profiles created from successively stronger lines (again, with multiplicative increments of $10^{0.5}$) is also shown in Figure 7 (*lower solid lines*).

The weakest lines observed for $J = 3$ have $\log f\lambda \sim 0$ and an *apparent* maximum $\log N(H_2) = 10^{14.85}$ cm^{-2} (km s^{-1})$^{-1}$. In Figure 7 this condition corresponds to a curve midway between the first and second lines at the top, since the apparent τ_0 is $10^{0.27}$. At the other extreme, the strongest lines have log $f\lambda \sim 1.25$, and they should match the third lowest line in Figure 7. At 6 km s^{-1} away from the center of the line cluster, the disparity between the two curves equals $10^{0.28}$. This difference is about equal to the vertical distance between the lightest and boldest curves in Figure 6*b* at heliocentric velocities of -23.4 and -11.4 km s^{-1}. Even larger differences are seen for $J = 2$ because the optical depths are greater at these velocity points. Thus, we have shown quantitatively that we can synthesize a model for a complex velocity distribution for the H_2 which duplicates the disparity in our constructions of column density

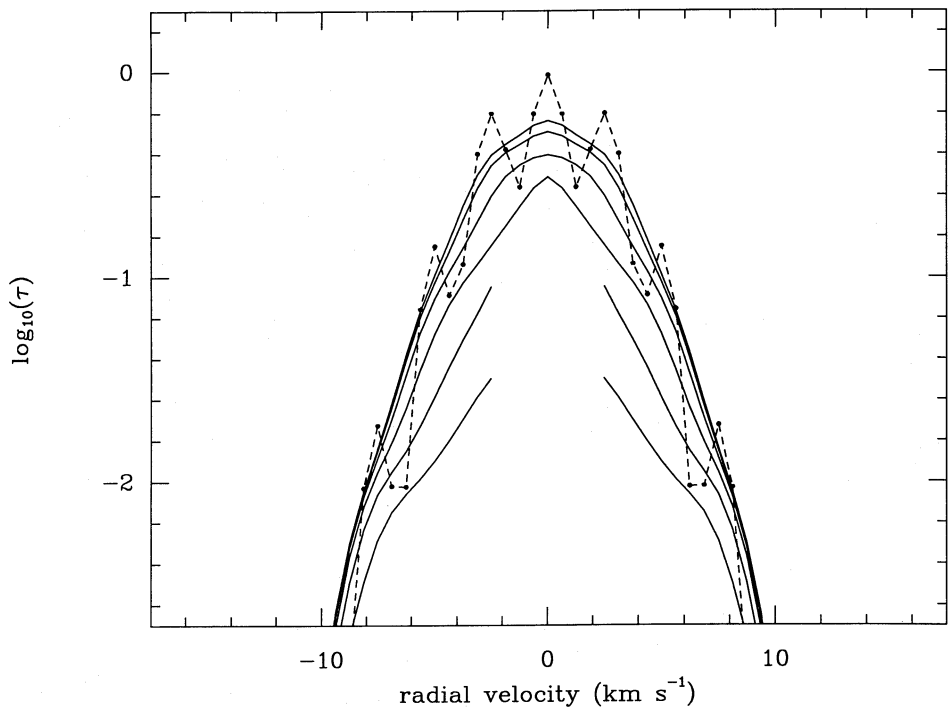

FIG. 7.—Expected outcome for the model cluster of narrow profiles defined in § IV*e*, assuming that the absorption features were smeared by the (worst case) IMAPS instrumental profile, converted to $\tau(v)$, and then plotted in the manner of Fig. 6. The dashed line shows what we would have obtained if our resolving power were perfect, except for the binning of intensities in individual cells ($=\frac{1}{2}$ CCD pixel in width). The topmost solid line shows how this profile is altered by smoothing, while the remaining solid lines apply to absorption lines which are successively stronger in τ by logarithmic increments of 0.5 dex. The artificial vertical translations of the curves to reverse these logarithmic changes would have made the solid curves coincident with each other, were it not for the corruption of τ derivations for saturated lines by the instrumental smoothing.

per unit velocity, assuming that our instrumental profile is about as broad as our worst-case estimate.

Total equivalent widths for the model line aggregate saturate in a manner corresponding to $b = 3.3$ km s^{-1} at log $(W_\lambda/\lambda) = -4.5$ (b increases very slightly for higher levels of saturation). Spitzer, Cochran, and Hirshfeld (1974) characterized the growth of lines from all J levels using a standard curve of growth with $b = 3.8$ km s^{-1}. Our model appears to be in satisfactory agreement with their observations.

f) *Comparisons of Profiles for Different J*

In the previous section, we learned that probably all but the weakest lines out of $J = 2$ and $J = 3$ are unsuitable for depicting τ at the resolution of IMAPS. For $J = 4$, all lines of different strength seem to agree, so it is probably safe to assume that the misrepresentations of the smoothed τ's are nonexistent for this and the $J = 5$ level. Furthermore, the *apparent* central optical depth of the *strongest* line for $J = 4$ is about equivalent to that of the *weakest* line for $J = 3$.

Figure 8 shows a consolidation of information from the weakest profiles in Figures 6*a* and 6*b* and all of the lines shown in Figures 6*c* and 6*d*. To derive these curves, we performed a maximum-likelihood analysis[4] for the useful portions (as defined in § IV*d* above) of all observations at each velocity. The likelihood functions for individual recordings of τ were computed from the combined errors arising from baseline uncertainties, misplacement of continua, and noise in the intensities (see § IV*e*).

To validate our error estimates, we measured at each velocity the χ^2 values for the departures of individual observations from the adopted composite curve. Except for the right-hand half of the $J = 2$ curve, the sums of χ^2 were less than the number of degrees of freedom ($n_{obs} - 1$). From the standpoint of *random* processes which could influence intensities, baselines, or continua, this analysis indicated that our error estimates were not only fair but perhaps even too conservative. The representative separation in velocity between significant changes in the χ^2 sums also indicated that the separation of statistically independent measurements is about 1 CCD pixel. This finding demonstrates that there was no significant cross-talk between adjacent CCD pixels during the analog signal transmission or digitization of the data. Our earlier estimate for the coherence length of errors was indeed reasonable.

Except for $J = 2$, we evaluated how well different parabolas fitted the profiles shown in Figure 8 by exploring acceptable combinations of the three parameters which define a second-degree equation. Our criterion for the goodness of fit was the sum of χ^2 over the velocity interval of each profile. The last two columns in Table 8 indicate that a parabola gives a satisfactory fit to the data for $J = 5$, but the minimum χ^2 values we could obtain for $J = 3$ and $J = 4$ showed that there are discernible departures from a purely parabolic form (at significance levels of 87% and 99.9%, respectively). One can easily recognize the significant asymmetry for the $J = 4$ profile. In the discussion which follows in this section and in § V, however, we regard the departures as inconsequential.

For a given J level, the width of a best-fit parabola and the

[4] Were it not for asymmetries in the errors, this would be equivalent to a weighted least-squares solution.

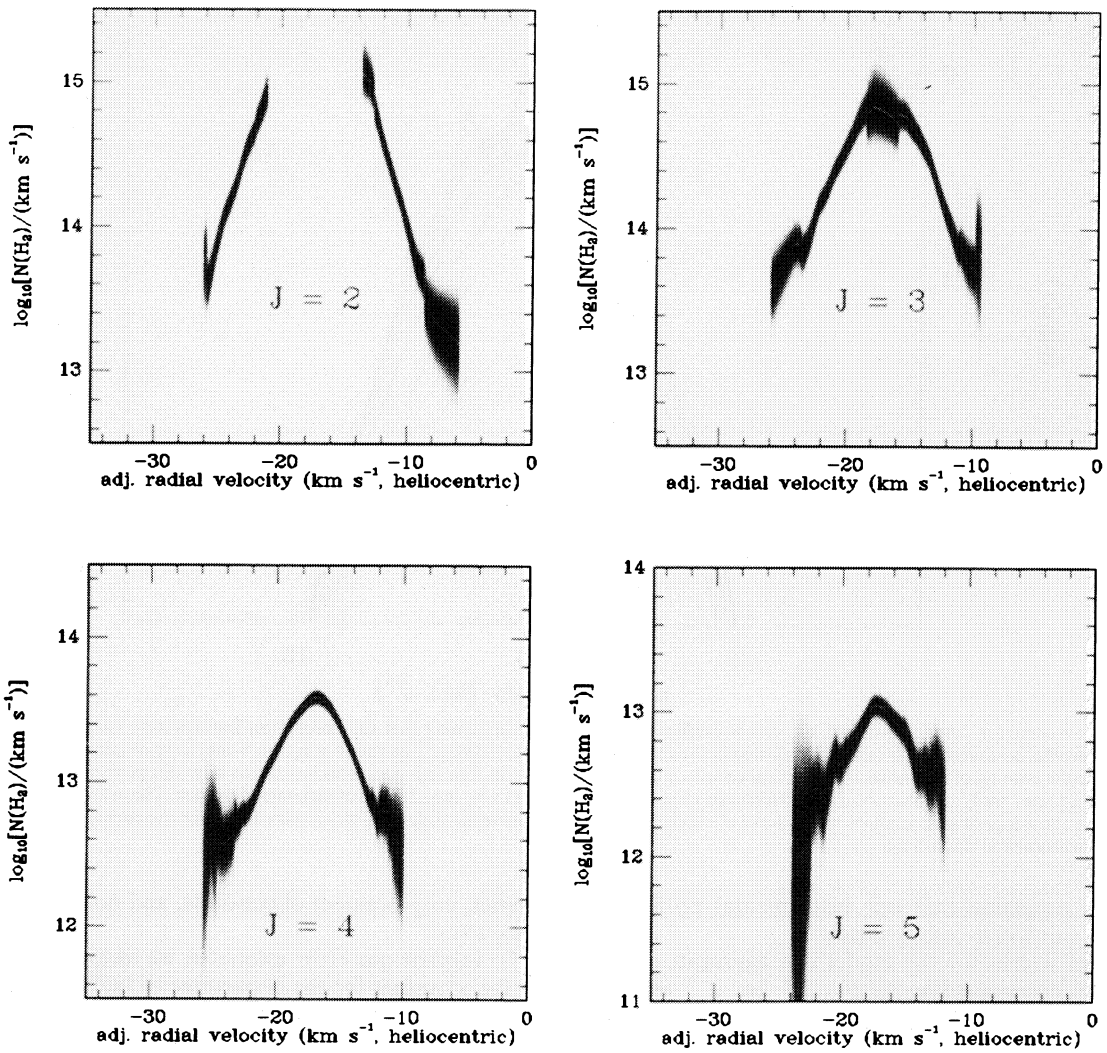

FIG. 8.—Composites of velocity profiles, plotted logarithmically, for H_2 in four different stages of rotational excitation. These curves and their accompanying error envelopes were derived from the lines shown in Fig. 6, excluding those which were plotted with bold markers (i.e., lines with $\log f\lambda > 0.5$ for $J = 2$ and $J = 3$). The extrema in the error envelopes represent approximately the $\pm 2\,\sigma$ limits. Discontinuities are the result of there being different numbers of lines to use over different velocity intervals.

TABLE 8

H_2 OPTICAL DEPTH PROFILES: TOTAL COLUMN DENSITIES AND VELOCITY WIDTHS
(90% confidence intervals)

	$N(H_2)$ (cm^{-2})			σ (km s^{-1})			GOODNESS OF FIT	
J[a]	Lower Limit	Preferred Value	Upper Limit	Lower Limit	Preferred Value	Upper Limit	χ^2_{min}	d.f.[b]
3[c]	15.66	15.71	15.77	3.00	3.21	3.43	13.0	8.2
4	14.34	14.37	14.40	2.69	2.82	2.96	26.7	8.2
5	13.75	13.83	13.93	2.24	2.59	3.24	3.3	5.0

[a] See Table 7 for lines used to define the composite profile.
[b] Degrees of freedom (d.f.) = $n - 3$, where n is the number of independent velocity measurements.
[c] For $J = 3$, only lines with $\log f\lambda < 0.5$ were used. The three column densities for this J level were raised by 0.05 dex above those indicated by the best-fit parabolas, to correct for the small, systematic errors in the smoothed optical depths.

height of its vertex indicate the total column density $N(H_2)$.[5] Three columns in Table 8 show the preferred $N(H_2)$ values and the corresponding 90% confidence intervals, based on limits for the expected distribution of χ^2 with 2 degrees of freedom for all possible combinations of the three parameters. Our values agree favorably with the determinations log $N(H_2\ J = 3) = 15.74$, log $N(H_2\ J = 4) = 14.28$, and log $N(H_2\ J = 5) = 13.79$ given by Spitzer, Cochran, and Hirshfeld (1974). (Their error estimates for the column densities in $J = 3$ and $J = 4$ are somewhere between 0.10 and 0.19 dex, and for $J = 5$ the uncertainty is between 0.04 and 0.09 dex.)[6] Table 8 also shows preferred and limiting values for the widths of parabolas, expressed in terms of the standard deviation σ of the Gaussian velocity profile. Here, we considered the x- and y-coordinates of the vertices as irrelevant parameters and thus used the confidence intervals corresponding to a χ^2 distribution with only 1 degree of freedom.[7]

The numbers for σ in the table show an important conclusion: The most probable values for the velocity widths become progressively smaller as J increases, and the difference in widths for $J = 3$ and $J = 4$ is statistically significant (the fact that the 90% confidence intervals do not overlap indicates the probability that $\sigma_{J=3} \leq \sigma_{J=4}$ should be less than 0.0025). We acknowledge that large disparities in $N(H_2)$ from one J level to the next create significant differences in line strengths from group to group, and one might question whether some unknown systematic effect could deceive us into thinking the profiles were different when indeed they were not. As noted earlier, however, there is an overlap in the strengths of some of the $J = 3$ and $J = 4$ lines. It is reassuring to see that the average values of $\langle v - \bar{v} \rangle^2$ for the Lyman 0–0 $P(3)$ and $R(3)$ intensity profiles are greater than those of the Lyman 4–0, 5–0, and 6–0 $R(4)$ transitions by an amount which is consistent with the square of the ratios of the respective σ's given in Table 8.

V. MODELS OF THE H_2 EXCITATION IN THE π SCO CLOUD

Models of the interstellar matter along the line of sight toward π Sco need to explain at least two aspects of the observational data presented in § IV: first, the total column densities in the various H_2 rotational levels, and, second, the measured line shapes, in particular the observation that the lines appear to become narrower as J increases from 3 to 5.

Two basic mechanisms are usually invoked to explain the rotational population distributions of H_2 in diffuse clouds: ultraviolet pumping through absorptions in the Lyman and Werner systems followed by fluorescence and infrared cascade (Spitzer and Zweibel 1974; Black and Dalgarno 1973, 1977; Jura 1975*a*, *b*) and collisional excitation in a gas heated by shocks (Aannestad and Field 1973; Draine and Katz 1986; Pineau-des-Forêts *et al.* 1986). We will consider first the ultraviolet excitation mechanism.

a) Homogeneous Steady State Models

Plane-parallel, steady state models of the fluorescent excitation of H_2 in diffuse clouds have been developed most recently by van Dishoeck and Black (1986, hereafter vDB) and by Viala, Roueff, and Abgrall (1988). These models calculate at each depth into the cloud the balance between several processes: (1) the formation of the H_2 molecule on the surfaces of grains, (2) its destruction by photodissociation through discrete absorptions in the Lyman and Werner bands, (3) its simultaneous excitation by ultraviolet pumping followed by infrared cascade, and (4) its excitation and de-excitation through inelastic collisions with H and H_2, and through reactive collisions with protons. An important aspect of the models is the treatment of the self-shielding in the absorption lines and the continuum shielding by dust for the ultraviolet Lyman and Werner transitions through which both the photodissociation and the excitation occur.

We follow here the procedure outlined by vDB, and investigate first the possibility that the cloud has a homogeneous structure with values of the temperature T and density $n_H = n(H) + 2n(H_2)$ that are constant with depth. The other major parameter that enters the models is the strength of the interstellar radiation field incident on the cloud surface, which is specified by a scaling factor I_{UV}, where $I_{UV} = 1$ refers to the intensity of the unattenuated interstellar radiation field as given by Draine (1978). Parameters of lesser importance are (1) the scattering properties of the grains at ultraviolet wavelengths; (2) the adopted formation efficiency of H_2 on grains, specified by a scaling factor y_f such that the formation rate is $3 \times 10^{-18} T^{1/2} y_f n_H n(H)$ cm^{-3} s^{-1}; (3) the model that is employed for the initial population distribution over the vibration-rotation levels of the newly formed H_2 molecules on grains, designated by φ; (4) the Doppler parameter b that is used in the calculation of the self-shielding in the ultraviolet absorption lines of H_2; (5) the rate coefficients that are adopted for the collisional processes; and (6) the cosmic-ray ionization rate ζ_0, which determines the proton concentration. Unless indicated otherwise, the H-H_2 collisional rates of Green and Truhlar (1979) are used, together with the H_2-H_2 rates of Allison and Dalgarno (1967) and the H^+-H_2 proton exchange rates of Black and Dalgarno (1977). The cosmic-ray ionization rate is kept at 5×10^{-17} s^{-1} throughout, based on the results of vDB. In the vDB models, the total H_2 column density is fixed and is taken equal to the observed value.

As discussed by vDB, the populations of the higher rotational levels $J \geq 4$ are sensitive primarily to the strength of the ultraviolet radiation field in the cloud, whereas the population distribution over the lower levels, $J = 0$ to $J = 2$, reflects the temperature structure in the cloud. The abundance ratio of H_2 with respect to H depends on the combination of parameters $n_H y_f / I_{UV}$. Thus T, n_H, and I_{UV} can be determined from the observed H and H_2 observations alone. The atomic hydrogen column density toward π Sco has been measured by Savage *et al.* (1977) from the damped Lyα profile to be $N(H) = (5.2 \pm 0.5) \times 10^{20}$ cm^{-2}. However, 21 cm observations by Cappa de Nicolau and Pöppel (1986) show that only half of the H atoms in front of the star have velocities in the range $v_{helio} = -23$ to -13 km s^{-1}, where the H_2 absorption occurs.[8] Accordingly, we have used $N(H) = (2.0 \pm 0.7) \times 10^{20}$ cm^{-2} in our models.

[5] For two reasons we prefer this method for measuring $N(H_2)$ over a direct integration of the optical depth profile: (1) the interpretation of errors is straightforward and (2) the result gives an extrapolation of a Gaussian velocity curve outside the measurement interval. For $J = 4$, where there is a noticeable departure from the best-fit parabola, the value log $N(H_2) = 14.38$ obtained by direct integration is very close to the preferred value given in the table.

[6] Spitzer, Cochran, and Hirshfeld (1974) mislabeled π Sco as "τ Sco" in their Table 4.

[7] Errors in higher order (neglected) terms of the equation for the velocity profile are assumed to be uncorrelated with those of the three variables for the parabola. For a discussion on confidence intervals in parameter estimation see Lampton, Margon, and Bowyer (1976).

[8] In the direction of π Sco, one must add 8.8 km s^{-1} to the heliocentric velocity to obtain a velocity in the local standard of rest.

TABLE 9

HOMOGENEOUS MODEL H OF THE π SCO CLOUD[a]

Parameters and Species	Model[b]	Observations
n_H (cm^{-3})	100	...
T (K)	81	...
I_{UV}	3	...
H	20.30	20.30 ± 0.15[c]
H_2	19.32	19.32 ± 0.13[c]
H_2 $J = 0$	19.00	19.00 ± 0.2[c]
$J = 1$	19.05	19.04 ± 0.2[c]
$J = 2$	16.89	16.51 ± 0.29[d]
$J = 3$	15.69	15.71 ± 0.06[e]
$J = 4$	14.51	14.37 ± 0.03[e]
$J = 5$	13.82	13.83 ± 0.10[e]
$J = 6$	12.85	<13.99[d]
$J = 7$	12.21	...

[a] The table lists the logarithm of the column densities in cm^{-2}.

[b] The model uses grain model 2 of Roberge, Dalgarno, and Flannery 1981, $y_f = 1.8$, H_2 formation model $\varphi = 4$, $b = 1$ km s^{-1}, and $\zeta_0 = 5 \times 10^{-17}$ s^{-1}.

[c] Savage *et al.* 1977. Only the amount of H with velocities $v_{helio} = -23$ to -13 km s^{-1} is taken into account (cf. Cappa de Nicolau and Pöppel 1986).

[d] Spitzer, Cochran, and Hirshfeld 1974.

[e] This work.

In Table 9 the computed H_2 column densities are presented for the best-fitting homogeneous model of the π Sco cloud. We will denote this model as model H. The temperature in the model is close to that suggested by the observed $J = 1/J = 0$ population ratio (Savage *et al.* 1977), 81 K. The density in the π Sco cloud must be low because of the relatively low proportion of hydrogen in molecular form. Additional support for a low density, $n_H < 150$ cm^{-3}, comes from the measured fine-structure populations of atomic carbon (Jenkins and Shaya 1979; see also § VI). The grain formation efficiency y_f is chosen to be of order unity. Although the H_2 formation rate has been inferred to be lower than average in the Ophiuchus cloud as a whole (Bohlin, Savage, and Drake 1978; Jura 1980; Snow 1983), these discussions do not yet take into account the possibility of a substantial population of small grains which may enhance the effective H_2 formation surface area. For $y_f = 1.8$, the inferred density is $n_H = 100$ cm^{-3}. The ultraviolet radiation field appears enhanced by a factor of about 3, if grain model 2 of Roberge, Dalgarno, and Flannery (1981) is adopted for the scattering properties of the grains. If their more forward-scattering grain model 3 is employed, I_{UV} can be lowered to about 1.5–2. The model presented in Table 9 is assumed to be illuminated on one side only. Results of models in which both sides are illuminated equally are very similar. We also found that variations in the adopted b parameter from 1 to 4 km s^{-1}, and in the cosmic-ray ionization rate ζ_0 from 10^{-17} to 10^{-16} s^{-1}, do not affect the results. The insensitivity to the value of b stems from the fact that the column densities in $J = 0$ and $J = 1$ are large enough that most of the pumping occurs in the Lorentzian wings of the lines originating from these levels.

Compared with observations, it appears that the homogeneous model can reproduce the measured column densities of H and H_2 in its various rotational energy levels very well: the differences are less than a factor of 2.5, and at most 1.4 if one does not include observationally uncertain $J = 2$. In fact, the agreement between the model and the observations is better for the π Sco cloud than for most other diffuse clouds studied so far, and strongly supports the ultraviolet pumping process as the primary mechanism for populating the excited rotational levels. However, the homogeneous model is incapable of explaining the observed decrease in line widths for higher J. In the following sections, we will therefore consider a series of inhomogeneous or "clumpy" models of the π Sco cloud.

b) Inhomogeneous or "Clumpy" Models

i) *Models with Constant Radiation Fields and Densities*

As explained in § IV, the $J = 3$ line profiles suggest that the interstellar matter toward π Sco actually consists of a number of narrow components which were not resolved by our instrument. A good fit to the $J = 3$ profiles was obtained with seven components, spaced 2.5 km s^{-1} apart and distributed symmetrically around the central velocity, with relative fractions and temperatures shown in Table 10. We will denote this model as model A. In the following, we will refer to the three components at 0 and ±2.5 km s^{-1} shifts as the "low-velocity" components, and the other four components at ±5 and ±7.5 km s^{-1} as the "high-velocity" components.

As discussed in § V*a*, the temperatures of 81 K for the low-velocity components were constrained mostly by the observed $J = 0$ and $J = 1$ population ratios. Since over 90% of the total H_2 column density is in these two components, their temperature should be close to that suggested by the ratio of ortho- to para-hydrogen in the entire cloud. No such requirements are imposed on the high-velocity clumps, but, as mentioned earlier, these components need to be narrow, and hence need to have low temperatures, $T < 60$ K. Since very low temperatures, $T < 20$ K, are unlikely in diffuse clouds, the range of temperatures for the high-velocity components is restricted to 20 K $< T <$ 60 K. We choose the median temperature $T = 40$ K to use in model A, but varying T in the range 20–60 K would have no significant effect on the model results.

In model A, the incident radiation field I_{UV} and density n_H were held constant between components. Thus, we assumed initially that the clumps do not shield each other and are exposed to the same outside radiation field. As before, the

TABLE 10

CLOUD MODEL A PARAMETERS[a]

Parameters	Component 1	2	3	4
Δv (km s^{-1})[b]	0	±2.5	±5	±7.5
T (K)	81	81	40	40
b (km s^{-1})	0.82	0.82	0.58	0.58
Fraction of H_2 $J = 3$[c]	0.40	0.26	0.035	0.0050
n_H (cm^{-3})	100	100	100	100
I_{UV}	1.3	1.3	1.3	1.3
H[d]	19.87	19.70	19.18	18.30
H_2[d]	19.06	18.66	17.10	14.32
Fraction of H_2	0.548	0.220	0.006	0.00001
Fraction of (H + $2H_2$)	0.398	0.243	0.064	0.008
Size (pc)	0.31	0.19	0.05	0.007

[a] The top part of the table lists the constraints on the model given by the $J = 3$ profiles; the lower part gives the inferred parameters. In all components, $y_f = 1.8$, and H_2 formation model $\varphi = 4$ was used.

[b] Velocity shift from central velocity.

[c] Fraction of total H_2 $J = 3$ column density in each component.

[d] Logarithm of column density in cm^{-2} in each component. The column densities for components 2–4 should be multiplied by 2 in order to obtain the total column density.

individual clumps were assumed to be illuminated on one side only. The value of I_{UV} was again determined by requiring that the model reproduce the H_2 column densities in the higher $J = 3$ to $J = 5$ levels. The closest fit to the $J = 3$ and $J = 5$ data was obtained with $I_{UV} = 1.3$, which is somewhat smaller than $I_{UV} = 3$ found in our homogeneous model. Evidently, breaking one big cloud into little clumps enhances the pumping, since most of the excitation arises from the boundary layers of a cloud or clump. This increase more than offsets the more rapid decrease in each cloud caused by the lower velocity dispersion. In model A, the size of the boundary layer is effectively increased compared with model H because the clumps are assumed not to shield each other. Thus a lower radiation field can reproduce the observed amount of rotational excitation. With $I_{UV} = 1.3$, the column density in $J = 4$ is overproduced by about 40%, and the best fit for that level was with $I_{UV} = 1.1$. However, the overproduction in $J = 4$ is probably just a consequence of the fact that the $J = 2$ population is too high in the models as well, rather than an indication of a lower incident flux (see also below).

As in model H, the density $n_H y_f \approx 180$ cm^{-3} in the clumps is constrained mostly by the observed ratio of atomic to molecular hydrogen. If we require $y_f < 3$, then 60 cm$^{-3} < n_H < 150$ cm^{-3}. Varying the central density within this range does not change the rotational populations by more than 10%. We adopt $n_H = 100$ cm^{-3}. With I_{UV} and n_H fixed, the total H_2 column density in each clump was subsequently constrained to reproduce exactly the relative fraction of H_2 in $J = 3$ derived from observations.

The resulting column densities in model A are summarized in Table 11 and are found to reproduce the observed abundances moderately well. The largest discrepancy is found for the $J = 2$ level, for which the model result is more than twice that which is observed. Note, however, that the error in the measured $J = 2$ column density is large because the central portions of the lines are strongly saturated, even for the weakest transitions that can be observed.

In order to investigate the sensitivity of the model results to other parameters, we ran a series of additional models, which are summarized in Table 12. It appears that the results for the π Sco cloud are quite insensitive to the adopted collisional rates, even though the H-H_2 rates are uncertain by an order of magnitude. Only the $J = 2$ and $J = 3$ populations are affected, by at most 20%. This is because at the densities and temperatures in the π Sco cloud, the $J = 0$ and $J = 1$ populations are completely thermalized, whereas the high J levels ($J \geq 4$) are populated almost entirely by the ultraviolet pumping process. It follows that $J = 2$ and $J = 3$ are intermediate in that their populations are governed by both collisional and radiative processes, so they have a stronger dependence on collisional rates.

Likewise, choosing a different H_2 formation model does not affect our interpretations of the observations significantly, as Table 12 shows. The formation model specifies how the 4.5 eV energy, released when a H_2 molecule forms on the surface of a grain, is distributed between the kinetic energy of the grain and the molecule, and the various modes of internal vibration-rotation energy of the molecule. The various models φ are given explicitly by Black and van Dishoeck (1987). In model $\varphi = 1$, one-third of the energy is deposited statistically as internal excitation of the newly formed molecule. In model $\varphi = 2$, 25% of the H_2 forms in $v = 14$, $J = 0$ and 75% in $v = 14$, $J = 1$ (Leonas and Pjarnpuu 1981). Model $\varphi = 3$, suggested by Duley and Williams (1986), assumes that all molecules initially enter level $v = 6$ with a distribution over the rotational levels J characterized by an effective formation temperature $T_f \approx T_{grain} \approx 15$ K. Finally, in model $\varphi = 4$, we suppose that 25% of the H_2 molecules originate in $v = 3$, $J = 0$ and 75% in $v = 3$, $J = 1$.

TABLE 11

COMPARISON OF MODEL RESULTS WITH OBSERVATIONS[a]

Species	Model A[b]	Model B[c]	Observed[d]
H	20.32	20.31	20.30 ± 0.15
H_2	19.32	19.32	19.32 ± 0.13
H_2 $J = 0$	19.00	19.01	19.00 ± 0.2
$J = 1$	19.04	19.03	19.04 ± 0.2
$J = 2$	16.87	16.86	16.51 ± 0.29
$J = 3$	15.65	15.65	15.71 ± 0.06
$J = 4$	14.51	14.47	14.37 ± 0.03
$J = 5$	13.82	13.82	13.83 ± 0.10
$J = 6$	12.86	12.84	< 13.99
$J = 7$	12.20	12.22	...
HD	13.29	13.11	13.13 ± 0.2[e]
C	12.91	12.94	12.91 ± 0.24[f]
C^+	16.02	16.31	...
CH	11.16	11.23	< 11.18[g]
CH^+	10.55	10.39	11.76[h]
C_2	9.66	10.25	...
OH	12.60	12.39	...
CO	11.29	11.89	11.95 ± 0.3[i]
NH	9.37	9.06	...
CN	9.36	9.24	...
Na	11.70	11.68	11.72[j]
Ca^+	10.35	10.39	< 10.50[k]
K	10.20	10.10	< 10.36[l]

[a] The table lists the logarithm of the column densities in cm^{-2} for each species.

[b] See Table 10 for the parameters of model A; the chemistry calculations used $\zeta_0 = 2.5 \times 10^{-17}$ s^{-1}, $\delta_D = 0.8$, $\delta_C = 0.09$, $\delta_O = 0.5$, $\delta_{Na} = 0.22$, $\delta_{Ca} = 1.6 \times 10^{-4}$, and $\delta_K = 0.17$.

[c] See Table 14 for the parameters of model B; the chemistry calculations used $\zeta_0 = 5 \times 10^{-17}$ s^{-1}, $\delta_D = 1.0$, $\delta_C = 0.18$, $\delta_O = 0.5$, $\delta_{Na} = 0.36$, $\delta_{Ca} = 3.2 \times 10^{-4}$, and $\delta_K = 0.25$.

[d] See Table 9 for references to the H and H_2 observations.

[e] Spitzer, Cochran, and Hirshfeld 1974.

[f] Jenkins and Shaya 1979.

[g] de Vries 1988, private communication.

[h] Lambert and Danks 1986.

[i] Federman *et al.* 1980; see also text in § VI.

[j] Hobbs 1974.

[k] Marschall and Hobbs 1972.

[l] Hobbs 1976.

Table 12 shows that the population distribution over the lower levels $J < 5$ is quite insensitive to the choice of the formation model. The largest differences are found for $J = 6$ and $J = 7$, which are populated up to 6 times more if model $\varphi = 1$ is adopted. Unfortunately, lines out of $J = 6$ and $J = 7$ were too weak to be detected toward π Sco. In fact, lines originating in $J \geq 6$ have so far been seen only toward a few stars, and are not yet able to distinguish uniquely between the various formation models. In the particular case of π Sco, we find that model $\varphi = 1$ consistently overproduces $J = 5$ relative to $J = 3$. Since model $\varphi = 4$ resulted in the best agreement with the observed $J = 3$ to $J = 5$ ratio, we adopted this model in all subsequent calculations. However, the existing data toward π Sco cannot exclude any of the other H_2 formation models.

In Figure 9 the model profiles are compared with the observed profiles. In this comparison, the model profiles were constructed in such a way as to mimic the observational procedure as closely as possible. For each velocity component,

TABLE 12

SENSITIVITY OF MODEL A RESULTS TO VARIOUS PARAMETERS[a]

PARAMETERS AND SPECIES	EXAMPLE 1	2	3	4	5	6	OBSERVED
H-H_2[b]	AD	GT	GT	GT	GT	GT	...
H^+-H_2[c]	BD	G	BD	BD	BD	BD	...
H_2 model φ[d]	4	4	4	1	2	3	...
H	2.06(20)	2.07(20)	2.08(20)	2.10(20)	2.08(20)	2.06(20)	(2.0 ± 0.7)(20)
H_2	2.10(19)	2.10(19)	2.10(19)	2.10(19)	2.10(19)	2.10(19)	(2.1 ± 0.7)(19)
H_2 $J = 0$	1.00(19)	1.01(19)	1.00(19)	1.00(19)	1.00(19)	1.05(19)	(1.0 ± 0.4)(19)
$J = 1$	1.10(19)	1.09(19)	1.10(19)	1.10(19)	1.10(19)	1.05(19)	(1.1 ± 0.4)(19)
$J = 2$	8.27(16)	7.47(16)	7.35(16)	7.42(16)	7.39(16)	9.19(16)	(3.2 ± 2.0)(16)
$J = 3$	3.75(15)	4.43(15)	4.47(15)	5.03(15)	4.56(15)	3.51(15)	(5.1 ± 0.7)(15)
$J = 4$	3.07(14)	3.25(14)	3.24(14)	3.65(14)	3.31(14)	4.28(14)	(2.3 ± 0.3)(14)
$J = 5$	6.47(13)	6.57(13)	6.61(13)	1.13(14)	7.07(13)	5.28(13)	(6.8 ± 1.5)(13)
$J = 6$	7.10(12)	7.23(12)	7.20(12)	1.26(13)	7.73(12)	9.50(12)	< 1(14)
$J = 7$	1.56(12)	1.57(12)	1.58(12)	8.72(12)	1.89(12)	1.30(12)	...
$J = 3/J = 5$	58.0	67.4	67.6	44.5	64.5	66.5	95.6

[a] The table lists the column densities in cm^{-2}; see Table 9 for references to the observed values. Numbers in parentheses are powers of 10.

[b] Adopted H-H_2 collisional rates. GT = Green and Truhlar 1979; AD = Allison and Dalgarno 1967.

[c] Adopted H^+-H_2 collisional rates. BD = Black and Dalgarno 1977; G = Gerlich 1988, cited in Roueff 1988.

[d] Adopted H_2 formation model φ. See Black and van Dishoeck 1987 and the text in § V for details of the models.

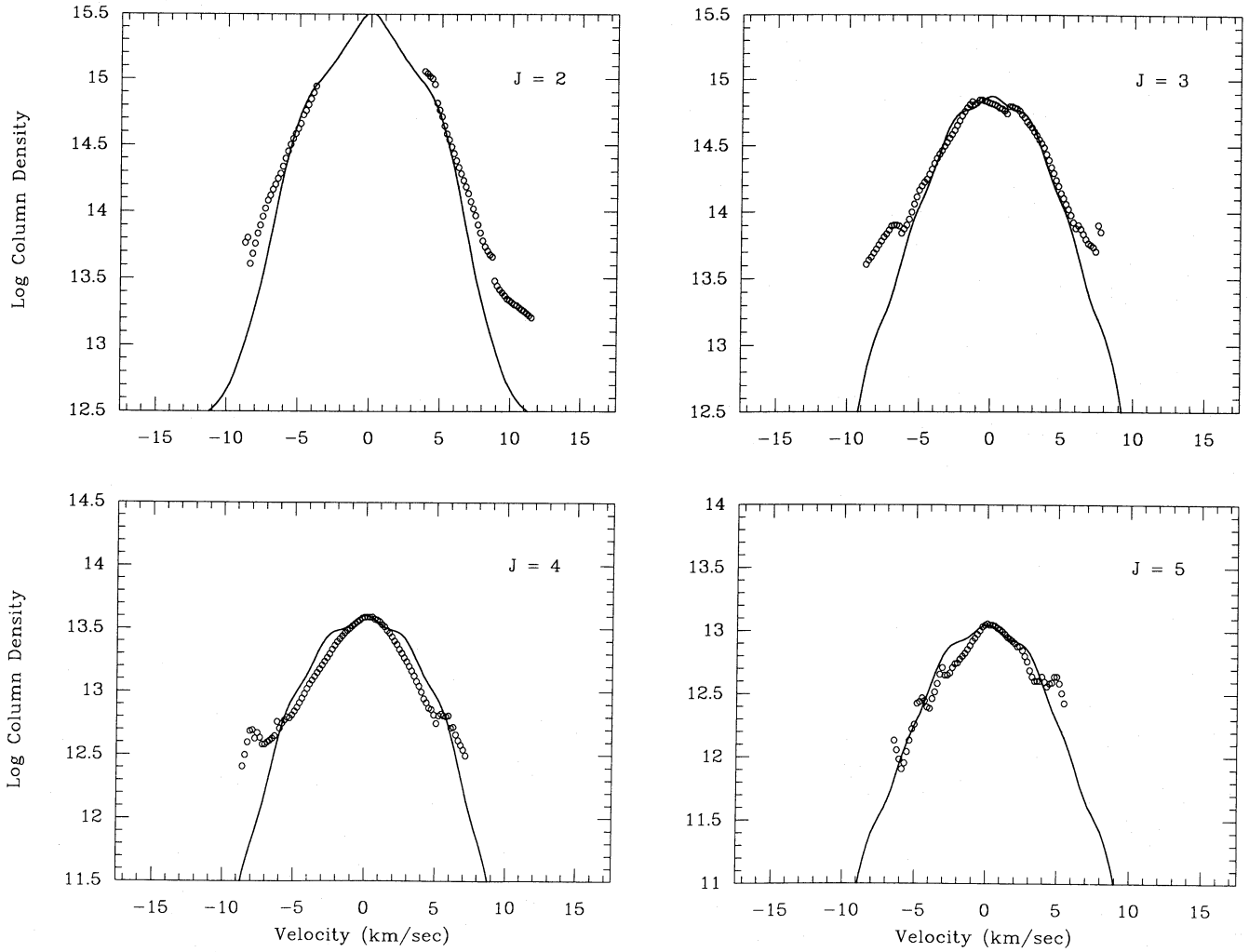

FIG. 9.—Comparison of observations shown in Fig. 8 (*circles*) against a reconstruction based on the results from Model A (*solid line*). This model assumes that all of the H_2 clumps at different velocities are exposed to the same intensity of *UV* starlight which optically pumps the H_2 into high-*J* levels.

absorption-line profiles for each level J were computed using the column densities found in the models. The profiles were then blended together with a Gaussian function having the same width as the instrumental profile, and column densities as functions of velocity were rederived from these profiles in the same way that the column densities had been rederived from the observed line profiles. Thus, the curves in Figure 9 do not represent true column density but rather the column density distribution that is obtained by the inferred optical depths per unit velocity, which are not quite valid (see § IV*d*). Also, since there exists the aforementioned disparity between the weak and strong lines in $J = 2$ and $J = 3$, and since the observed line profiles plotted in Figures 8 and 9 are a composite of only the weaker lines, we also used only weak lines, in particular the Lyman (0, 0) $R(2)$ and $R(3)$ lines, in our derivation of the model curves. The model profiles have been shifted vertically (by no more than 0.18 dex) to compensate for the fact that the model does not reproduce total column densities exactly.

As Figure 9 shows, the $J = 3$ model profile fits the observed points very well, as is to be expected, since this profile was a constraint on the model. However, it is clear that the model profile is too narrow for $J = 2$, and too wide for $J = 4$ and $J = 5$, as can be seen by comparing the curves in Figure 9 with the error envelopes shown in Figure 8. It appears that the column density at ± 5 and ± 7.5 km s^{-1} needs to be increased for the $J = 2$ level, and to be decreased at ± 2.5 and ± 5 km s^{-1} for $J = 4$ and $J = 5$. Table 13 shows the fractional contribution of each component to each rotational level. It clearly demonstrates that for model A the profiles become wider with higher J. This results from the fact that the self-shielding in the ultraviolet pumping lines is much larger in the low-velocity clumps which have the largest H_2 column densities. This conclusion does not agree with the observation that the composite line profiles appear to become narrower as J increases.

ii) *Models with Varying Radiation Fields and Densities*

From model A, we concluded that in order to better fit the profiles from $J = 2$, 4, and 5, the low-velocity components need to contribute more to the populations of the higher J levels, and the high-velocity components more to those of the lower J levels. The only way to achieve this is to have more pumping in the low-velocity components, and less in the high-velocity ones. In other words, the clump with lowest velocity shift must be closest to the outer edge of the cloud, and hence shields the other clumps from the radiation, which is assumed to be incident from one side only. Some shielding of the high-velocity components by the zero-velocity one is not unlikely, since the damping wings of lines out of $J = 0$ and $J = 1$ (through which most of the pumping occurs) are so wide that the radiation field is significantly reduced even far from the line center.

A proper model of the situation described above should not only include the self-shielding in the ultraviolet absorption lines in each clump but should also treat the partial shielding of each line in each clump by the corresponding line(s) in the zero-velocity clump. In addition, the various high-velocity clumps may shield each other, depending on geometry. Since our model assumes plane-parallel symmetry for each component, and thus cannot realistically simulate the three-dimensional distribution of the various clumps, such detailed shielding calculations are beyond the scope of this paper; they may, however, be presented in a future article. Instead, we take here the highly simplified approach in which the shielding by the low-velocity components is mimicked by an overall reduction in the strength of the radiation field incident on the high-velocity clumps.

We therefore developed a new model, model B, with the same number of components as model A, but in which the incident ultraviolet flux could vary from clump to clump. Because of the sensitivity of the high-J populations to the ultraviolet flux, the scaling factors I_{UV} for each clump could be constrained quite well. The best fit was obtained when the clump at zero velocity shift had $I_{UV} \approx 3.6$. Because the incident radiation field is large in this case, both the ultraviolet pumping and the photodissociation are very efficient. As a result, the clump consists mostly of atomic hydrogen, and its fraction of total H_2 column density is quite small as Table 14 shows—only 7%. Nevertheless, estimates of the amount of shielding by the damping wings of lines out of $J = 0$ and $J = 1$ suggest that the column density of H_2 in the zero-velocity component is indeed sufficient to reduce the radiation field at velocity shifts of 2.5 km s^{-1} from line center to about 20% of its original value. However, if I_{UV} were increased from 4 to 10, the H_2 column density in component 1 would be too small to shield the other components by the required amounts. We estimate that the radiation field incident on the zero-velocity clump can be anywhere from 3 to 6 times the average interstellar value for the model to be internally consistent. The clumps at ± 5 and ± 7.5 km s^{-1} can, of course, also be shielded effectively by the large H_2 column densities in the ± 2.5 km s^{-1} components. We arrived at final incident fluxes of $I_{UV} \approx 1$ for the clumps at ± 2.5, and $I_{UV} \approx 0.3$ for the clumps at ± 5 and ± 7.5 km s^{-1}.

TABLE 13

FRACTIONAL CONTRIBUTION[a] FROM EACH COMPONENT TO H_2 J COLUMN DENSITY

	Model A Component				Model B Component			
Level	1	2	3	4	1	2	3	4
$J = 0$	0.55	0.22	0.009	8.0(−7)	0.05	0.21	0.27	0.001
$J = 1$	0.55	0.22	0.003	1.0(−5)	0.08	0.32	0.14	0.0008
$J = 2$	0.44	0.24	0.037	0.0004	0.27	0.31	0.052	0.0035
$J = 3$	0.40	0.26	0.035	0.0050	0.40	0.25	0.046	0.0063
$J = 4$	0.37	0.25	0.064	0.006	0.40	0.22	0.070	0.011
$J = 5$	0.38	0.25	0.046	0.011	0.42	0.23	0.051	0.0097
$J = 6$	0.36	0.25	0.069	0.007	0.45	0.20	0.062	0.011
$J = 7$	0.37	0.25	0.049	0.012	0.45	0.22	0.047	0.009

[a] The values for components 2–4 should be multiplied by 2 to obtain the total contribution on either side of the zero-velocity core of the group. To relate numbers for different J to each other, one must renormalize using the total column densities for each J level specified in Table 11.

TABLE 14

CLOUD MODEL B PARAMETERS[a]

PARAMETERS	COMPONENT 1	2	3	4
Δv (km s^{-1})[b]	0	±2.5	±5	±7.5
T (K)	100	100	60	60
b (km s^{-1})	0.91	0.91	0.70	0.70
Fraction of H_2 $J = 3$[c]	0.40	0.25	0.046	0.0063
n_H (cm^{-3})	75	75	300	300
I_{UV}[d]	3.6	1.0	0.31	0.36
H[e]	19.99	19.68	18.60	17.79
H_2[e]	18.15	18.75	18.62	16.32
Fraction of H_2	0.067	0.265	0.200	0.001
Fraction of (H + $2H_2$)	0.408	0.243	0.051	0.003
Size (pc)	0.43	0.26	0.01	7.0(−4)

[a] The top part of the table lists the constraints on the model given by the $J = 3$ profiles; the lower part gives the inferred parameters. In all components, $y_f = 1.9$, and H_2 formation model $\varphi = 4$ was used.

[b] Velocity shift from central velocity.

[c] Fraction of total H_2 $J = 3$ column density in each component.

[d] The values of I_{UV} for components 2–4 apply only to the calculation of the H_2 abundance and excitation. See § VI for the appropriate values for use in the chemistry.

[e] Logarithm of column density in cm^{-2} in each component. The column densities for components 2–4 should be multiplied by 2 in order to obtain the total column density.

Initially, the other parameters were kept fixed while the incident fluxes were varied. However, because of the reduced pumping in the higher velocity components, their total column densities had to be increased in order to reproduce the constraints provided by the $J = 3$ profile. About 53% of the total H_2 column density needs to be at ±2.5 km s^{-1}, 40% at ±5 km s^{-1}, and 0.2% at ±7.5 km s^{-1} in model B, compared with 44%, 1.2%, and 0.002% for model A (see Tables 10 and 14).

If most of the H_2 column density indeed resides in the ±2.5 and ±5 km s^{-1} components, the temperature structure needs to be adjusted as well, in order to reproduce the average temperature of 81 K given by the observed $J = 1$ to $J = 0$ abundance ratio. Temperatures of 100 and 60 K for the low- and high-velocity components, respectively, rather than 80 and 40 K, were also found to be consistent with the $J = 3$ line profiles (cf. § IV*e*) and reproduced well the correct ratio for the $J = 0$ and $J = 1$ total populations.

We also considered varying the central density from clump to clump, which affects mainly the $J = 2$ population. In the low-temperature clumps, the $J = 0$ level, and consequently also the $J = 2$ level, are relatively more populated than in the high-temperature clumps. Since in the low-T components the $J = 2$ level is overpopulated relative to the thermal equilibrium value, increasing the central density in these clumps decreases the population in $J = 2$. In the high-T clumps, where the $J = 2$ level population is subthermal (even though there is more rapid pumping), an increase in density increases the $J = 2$ abundance. Since model A overproduced the $J = 2$ population by a factor of 2, and the higher temperature in the low-velocity clumps would be expected to increase it still further, the density in the high-velocity components was increased, and that in the low-velocity clumps decreased in order to lower the $J = 2$ population. We chose $n_H = 75$ cm^{-3} for the low-velocity components and $n_H = 300$ cm^{-3} for the high-velocity clumps, and adjusted the formation efficiency y_f so as to reproduce the atomic hydrogen data. As will be shown in § VI, this density distribution is still consistent with the atomic carbon fine-structure excitation. Note that these densities are not tightly constrained, and that in fact any combination of densities $n_H < 1000$ cm^{-3} in the clumps is possible as long as the average density remains low. In particular, lowering the density in the high-velocity components to about 150 cm^{-3} affects the results for the H_2 excitation only slightly, although it would significantly reduce the production of other molecules.

The final parameters of model B are presented in Table 14, and it can be seen from Table 11 that the computed column densities match the observations quite well. Also shown, in Figure 10, are the model line profiles, which provide a much better fit to the observations than those for model A (as can be seen by comparing Figs. 9 and 10 with the error envelopes in Fig. 8) if the slight asymmetries in the observations are ignored. Table 13 illustrates that the profiles indeed become narrower with increasing J for model B, in agreement with the observational data.

c) A Possible Shocked Component?

The fact that the ultraviolet pumping mechanism reproduces very well the observed rotational population distribution of H_2 toward π Sco suggests that the amount of shock excitation of H_2 is small in this cloud. In addition, the $J = 3$ line profiles strongly indicate that the interstellar matter toward π Sco is composed of about seven narrow, cold components: a contribution from high-temperature gas of more than 20% to the $J = 3$ level population would wash out this structure. Since for most H_2 formation models, $J = 3$ is slightly underproduced relative to $J = 5$, a small amount of shock-heated gas (up to 20%) could contribute to this level without being in conflict with the models, as long as the warm gas does not populate levels as high as $J = 5$. However, a possible shocked component would also contribute to $J = 2$, making the fit for that level even worse. Another argument against a large shocked component is the absence of any systematic velocity shift

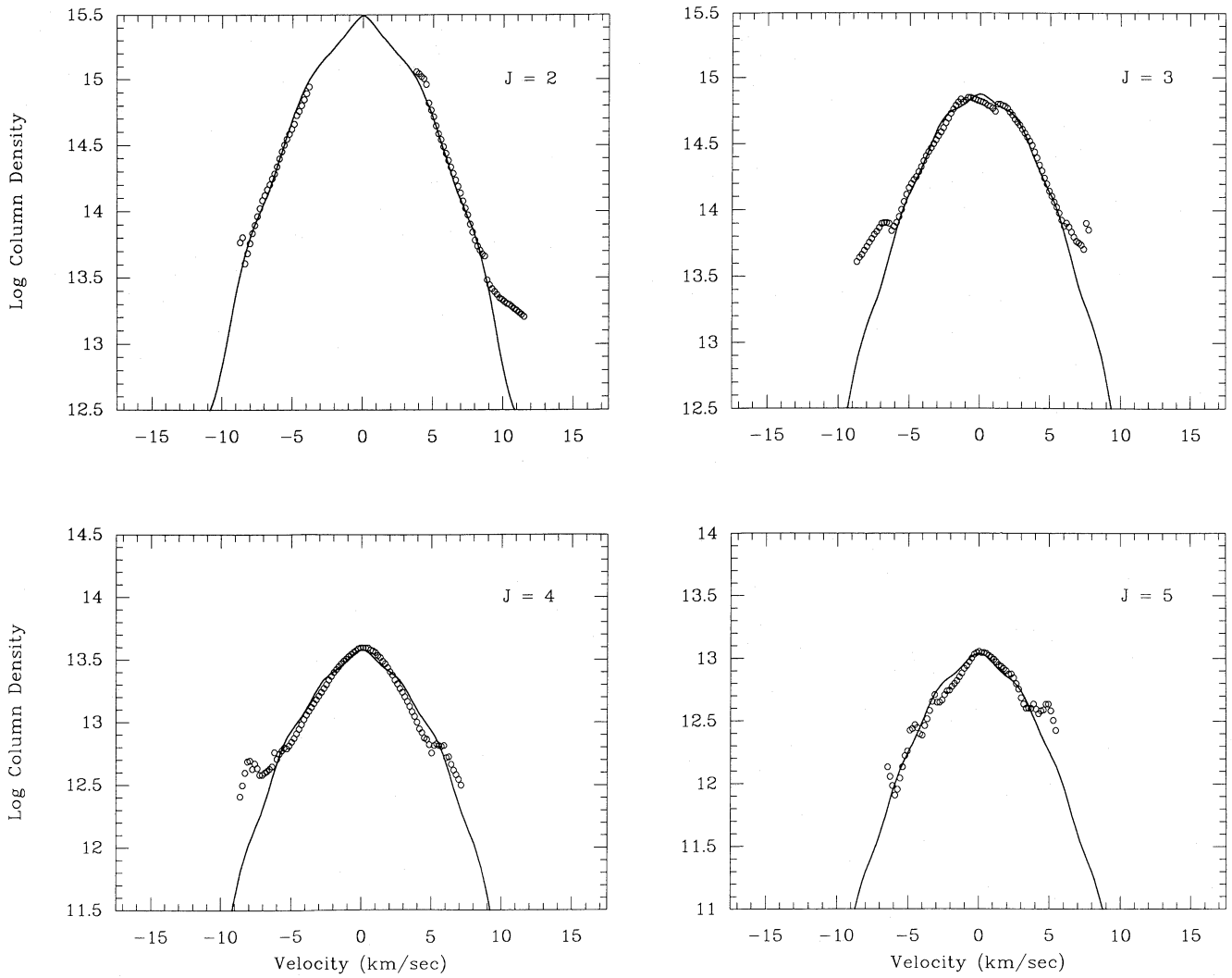

FIG. 10.—Comparison of observations shown in Fig. 8 (*circles*) against a reconstruction based on the results from model B (*solid line*). Model B differs from model A from the standpoint that the H_2 components near the edge of the profile are exposed to much less pumping radiation than those near the center. As a result, the computed profiles better duplicate the observed narrowing of the profiles for higher J.

between lines arising from levels $J = 0$ to $J = 5$ (cf. Table 7). Shock models (Elitzur and Watson 1980; Draine and Katz 1986) predict shifts between the quiescent and shocked gas of typically 2–3 km s^{-1}.

An argument in favor of a small shocked component is provided by the fact that CH^+ has been detected toward π Sco (Lambert and Danks 1986). It is well known that steady state, low-temperature models fail to reproduce the observed amounts of CH^+ in diffuse clouds (see also § VI) and that a region of enhanced temperature may be necessary to drive the $C^+ + H_2$ reaction which forms CH^+ (Elitzur and Watson 1978). A rough estimate of the amount of warm gas needed to reproduce the small amount of CH^+ observed in the π Sco cloud can be made from the formula presented by Lambert and Danks (1986):

$$\frac{N(CH^+)}{N(H_2)} = a \frac{N(H_2)_w}{N(H_2)},$$

where $a \approx 7 \times 10^{-6}$ for $T = 1000$ K and $a \approx 1 \times 10^{-4}$ for $T = 3000$ K. With $N(CH^+)/N(H_2) = 2.8 \times 10^{-8}$, the inferred population of warm hydrogen is $N(H_2)_w/N(H_2) \approx 0.004$ at $T = 1000$ K and 2.8×10^{-4} at 3000 K. The resulting column densities in $J = 3$ due to collisional excitation in the warm gas are 2.5×10^{16} and 1×10^{15} cm^{-2}, respectively, which can be compared with the total observed value of 6.5×10^{15} cm^{-2}. Note, however, that this estimate does not take into account the possibility of magnetic fields affecting the shock structure. In magnetohydrodynamic (MHD) shocks, the amount of warm hydrogen can be lowered, because the systematic velocity difference between the C^+ ions and H_2 molecules can assist the CH^+ formation reaction (Draine and Katz 1986; Pineau-des-Forêts *et al.* 1986). It would be of interest to develop MHD shock models that reproduce the observed CH^+ abundance in the π Sco cloud.

An interesting feature of the π Sco cloud is the fact that the CH^+ line profile, as presented by Lambert and Danks (1986), has a width of at most 2 km s^{-1}, which is much narrower than that of our H_2 line profiles. If there are no systematic errors in the radial velocities, the measured heliocentric velocity of -16.9 km s^{-1} for the CH^+ implies that it is formed mostly in the zero-velocity component. The contribution from this shock

to higher J levels, which are shifted by at most a few kilometers per second from CH^+, are thus also expected to arise mostly in the low-velocity components. Since the shocked gas typically will not be at a high enough temperature to populate the highest levels, such as $J = 4$ and $J = 5$, the addition of this narrow central component to the lines out of $J = 2$ and $J = 3$ will tend to make these line profiles even narrower than those of $J = 4$ and $J = 5$, a fact which is certainly not borne out by the observations.

In conclusion, both the H_2 $J = 2$ and $J = 3$ populations and their line profiles, as well as the absence of any systematic velocity shifts between the $J = 0$ to $J = 5$ lines, suggest that it is unlikely that there is a considerable shocked component along the line of sight to π Sco.

VI. ABUNDANCES OF OTHER SPECIES

A further test of the models can be made by a comparison of the theoretical results with observations of other species toward π Sco. The only other molecules that have been detected in the π Sco cloud are HD (Spitzer, Cochran, and Hirshfeld 1974), CO (Federman *et al.* 1980), and CH^+ (Lambert and Danks 1986). In addition, a handful of neutral atomic species have been seen.

Atomic and molecular abundances have been computed in our π Sco models using the chemical network described by van Dishoeck and Black (1986), but with an updated treatment of the CO photodissociation as described by van Dishoeck and Black (1988*a*, *b*). Special attention has to be paid to the appropriate strength of the radiation field for use in the chemistry in model B, since the values of I_{UV} listed in Table 14 for components 2–4 apply only to the calculation of the H_2 abundance and excitation. A strong decrease in I_{UV} is plausible in that case, because the damping wings of the saturated H_2 lines in component 1 can effectively shield the H_2 in the other components. However, this shielding is effective only in the 912–1100 Å region, and is obviously less significant for other molecules which photodissociate primarily at longer wavelengths, $\lambda > 1100$ Å. With the exception of CO, the other species will see a radiation field that is lowered only by the continuum extinction of the clumps in front of them, so that the appropriate incident fluxes for the chemistry calculations in model B are $I_{UV} \approx 3.2$, 2.9, and 2.9 for components 2–4.

The results for models A and B are included in Table 11. The computed HD abundance depends on two parameters in the models: the cosmic-ray ionization rate ζ_0 and the overall deuterium abundance $[D]/[H] = 1.5 \times 10^{-5}\delta_D$. Since the column density of HD in the π Sco cloud is too small for the ultraviolet lines to become optically thick, no shielding of the HD lines in components 2–4 by component 1 has to be considered. In addition, none of the H_2 lines in any of the components effectively shield the HD lines. Since model A easily produces too much HD compared with observations, either ζ_0 or δ_D, or both in combination, need to be lowered by a factor of about 2 compared with the reference values of $\zeta_0 = 5 \times 10^{-17}$ s^{-1} and $\delta_D = 1$ to bring the model into harmony with observations. In Table 11, $\zeta_0 = 2.5 \times 10^{-17}$ s^{-1} was chosen, together with $\delta_D = 0.8$. In model B, the HD is more effectively destroyed by the higher radiation field, so that in that model the reference values gave good agreement with observations.

The adopted cosmic-ray ionization rate also affects the computed OH abundance. Unfortunately, no observational data are available on the OH column density toward π Sco, but predicted column densities are included in Table 11.

The abundances of the carbon-bearing species in the π Sco cloud provide an interesting puzzle. The carbon chemistry depends strongly on the adopted carbon depletion factor δ_C, where $\delta_C = 1$ refers to an abundance of carbon in all forms of 4.7×10^{-4}. Although the dominant form of carbon is C^+ in diffuse clouds, the value of δ_C in the models is usually constrained by the observed neutral atomic carbon column density. Atomic carbon has been detected toward π Sco by Jenkins and Shaya (1979), but the observed column density is very small, only about 10^{13} cm^{-2}. In model A, carbon needs to be quite depleted, $\delta_C \approx 0.09$, in order to reproduce the observations. In model B, a larger fraction of the carbon is ionized because of the higher radiation field, so that δ_C can be raised to 0.18. The inferred values could be tested through measurements of the C^+ column density.

As mentioned in § V, the atomic carbon data also provide constraints on the density in the π Sco cloud. From the fact that no lines out of the excited $^3P_1$ fine-structure level were detected, Jenkins and Shaya (1979) concluded that $n_H T \leq 10^4$ cm^{-3} K. The chemical models used here compute explicitly at each depth the populations in the carbon fine-structure levels due to a variety of radiative and collisional processes listed by van Dishoeck and Black (1988*a*). In both models A and B, about 30% of the total atomic carbon population is in the $^3P_1$ level and about 6% in the $^3P_2$ level, which is consistent with the upper limits provided by the observations.

Given δ_C, the amount of CH in the models then depends on the adopted rate coefficient k_{ra} for the radiative association reaction between C^+ and H_2. If $k_{ra} = 5 \times 10^{-16}$ cm^3 s^{-1} (cf. van Dishoeck and Black 1986) is used, the computed CH column density in model A is more than 3 times less than the observed column density of 5×10^{11} cm^{-2} listed by Danks, Federman, and Lambert (1984). Note, however, that this column density is probably only an upper limit. Indeed, a more stringent limit on the equivalent width of the CH 4300 Å line of only 0.1 mÅ has recently been obtained by C. P. de Vries (1988, private communication) using the coudé echelle spectrometer equipped with a CCD detector on the coudé auxiliary telescope at the European Southern Observatory. This corresponds to an upper limit on the CH column density of 1.5×10^{11} cm^{-2}. In model B the higher gas-phase carbon abundance and the higher density in components 3 and 4 result in a CH column density close to the observed upper limit. As expected, the computed column densities of CH^+ in the steady state models fall below the observed value by more than an order of magnitude.

The production of CO in the models is similar to that of CH, in the sense that the larger gas-phase carbon abundance and the larger densities in the high-velocity components in model B increase the CO abundance significantly over that of model A. In model A, CO is underproduced by a factor of 4–5 compared with the observations of Federman *et al.* (1980). (However, reinspection of the original *Copernicus* data suggests that the detection is only quite marginal, and so the column density could possibly be lower by a factor of 2–3 than the value listed in Table 11.) On the other hand, the column density of CO produced in model B, where the shielding of CO at ultraviolet wavelengths by the H_2 lines is quite important, is very close to the observed value. However, since our model does not accurately treat the shielding of CO by the H_2 lines of other clumps, the column densities produced in the model can only be approximate values.

Another significant difference between models A and B is that in model A most of the molecules are concentrated in the

zero-velocity component, whereas in model B the molecules are found mainly in components 2 and 3. If the difference in densities between the low- and high-velocity components is indeed as large as assumed in model B, then about 70% of the CO and CH is produced in the ± 5 km s^{-1} components. Thus, the line profiles for these species would be expected to show a somewhat double-peaked structure. Unfortunately, the *Copernicus* data on CO are of too poor quality to test this theory. On the other hand, the line profiles of atomic species such as C and Na, as well as that of the CH^+ produced in steady state, are centrally peaked in model B, consistent with the observed profiles for these species (Hobbs 1969; Lambert and Danks 1986).

Observations of Na, Ca^+, and K toward π Sco have been published by Hobbs (1974), Marschall and Hobbs (1972), and Hobbs (1976). The measured column densities or upper limits can be reproduced in models in which these species are depleted by factors $\delta_{Na} \approx 0.36$, $\delta_{Ca} \leq 3.2 \times 10^{-4}$, and $\delta_K \leq 0.25$ with respect to the undepleted values listed by Lepp *et al.* (1988).

VII. DISCUSSION

Our study of the π Sco cloud raises the question of how ubiquitous are the qualitative features of the H_2 profile. In other words, are tight clusters of components whose widths are consistent with pure thermal Doppler broadening commonplace? The answer will probably be obtained only through H_2 observations of more lines of sight at similarly high resolution. There exists a large body of visible absorption-line data of molecules such as CH and CN at a resolution comparable to that of the ultraviolet data reported here. None of the profiles toward nearby stars show evidence for multiple structure in these molecules over a scale of 15 km s^{-1}. Only in the cloud toward ζ Oph have multiple molecular components been detected, since for this cloud the CO column density is large enough to allow millimeter observations. The millimeter data show that the ζ Oph cloud is composed of at least four clumps with velocities spanning a 3 km s^{-1} interval (Langer, Glassgold, and Wilson 1987). Note, however, that both the CH and the CN data, as well as the CO data, are sensitive only to quite large column densities of molecular gas with $N(H_2) > 10^{20}$ cm^{-2}. In such cases, the random superposition of many intricate substructures may be lost in the resulting bulk. This appears not to be the case near α Ori, where millimeter radio observations of CO by Knapp and Bowers (1988) have indicated the presence of isolated clouds with $n(H_2)$ ranging from about 40 to 300 cm^{-3}, diameters between 0.2 and 1 pc, and line widths of order 1 km s^{-1}. Such clouds are very similar to those which are responsible for the strong components that we observed near the center of the H_2 profile toward π Sco. In general, the ultraviolet H_2 observations can probe much smaller column densities of gas than the CH, CN, or CO observations, as do, for example, the atomic Na data.

It is well known that multiple components are a common occurrence in high-resolution Na profiles at visible wavelengths (see, e.g., Hobbs 1969; Blades, Wynne-Jones, and Wayte 1980; Crawford, Barlow, and Blades 1989). The width and position of the Na profile toward π Sco (Hobbs 1969) are very similar to those of our H_2 ensemble (the Na profile is centered at -15 km s^{-1}, while the molecular gas averages to -17.4 km s^{-1}). In addition, there is evidence for separate components at -22, -15, -12, and possibly -10 km s^{-1}. The overall appearance of the atomic Na profile differs, however, from that of the excited H_2 profiles, as discussed in § VI. Some multiplicity of components can also be distinguished in the Na I profiles toward stars not too distant from π Sco, such as δ Sco, β Sco, and σ Sco. To what extent these atomic components contain molecules is still an open question.

We next should try to interpret the significance of the seemingly organized and symmetrical arrangement of components with different physical conditions toward π Sco. To be sure, we cannot deny the possibility that we are viewing just a circumstantial superposition of unrelated entities. Nevertheless, we should not overlook the prospect that we are detecting the signature of a coherent system responding to some external influence or at least in some respect demonstrating an important principle for the dynamics of adjacent, possibly interacting, clouds.

Before we present some theoretical speculations, we need to address several considerations about the environment that we viewed. First, the factor of 3.6 enhancement of the UV radiation field for the zero-velocity component suggests that the cloud could be as close as 4–6 pc from π Sco itself, if the radiation from other, nearby stars were not important. This distance is comparable to the radius of the H II region around π Sco of about 3 pc (Sharpless 1959), if the distance to π Sco is taken to be 133 pc (de Geus, de Zeeuw, and Lub 1988). Next, except for an isolated gas cloud noted below, the direction toward π Sco is in a void within the vast, dense complex of gas connected with the Sco-Cen association. The average heliocentric velocity of the molecular gas toward π Sco of -17.4 km s^{-1} corresponds to $\bar{v}_{LSR} \approx -8.5$ km s^{-1}, which differs significantly from $\bar{v}_{LSR} \approx 0$–5 km s^{-1} found for the molecular material in the ρ Oph cloud from a CO millimeter emission survey (de Geus, Bronfman, and Thaddeus 1988). It also differs by -5 km s^{-1} or more from the interstellar matter seen toward, e.g., β Sco, δ Sco, and σ Sco, suggesting strongly that the π Sco cloud is a local phenomenon. Contour maps of 21 cm emission shown by Cappa de Nicolau and Pöppel (1986) for H I at nearly the same velocity as our H_2 profile (their component I′) indicate that we are looking through an isolated condensation of gas having an average H I column density of 9×10^{19} cm^{-2} and a diameter of about 7° (cf. their Table 5 and Figs. 9 and 17). This 21 cm emission probably comes from clouds of the type which make up our H_2 profile, but there may also be a contribution from a slightly hotter matrix of mostly atomic gas which supplies the external pressure to confine the much denser, cool H_2 clumps. Finally, Cappa de Nicolau and Pöppel (see also de Geus 1988) pointed out that this position is near the center of an expanding shell of gas, with a diameter of 27°, which has an estimated age of about (2–6) $\times 10^6$ yr, depending on assumptions about its origin (explosion or steady mass flow).

Let us now suppose that the H_2 clumps are *well inside* the large ring, i.e., they are not just appearing in projection. As suggested by Cappa de Nicolau and Pöppel (1986), the ring is probably material dredged by a shock in the snowplow phase of expansion. It is then reasonable to presume that several million years ago the shock may have slammed into the H_2 clumps and their supporting matrix. The ram pressure in the early phases of such an interaction would have flattened the dense complex somewhat. A short time later, when the shock had overtaken the material, the overall increase in pressure on the front and rear surfaces compressed the complex further, created converging isothermal shocks, and probably accelerated some of the embedded denser clumps inward. The larger clumps were probably not affected as much as the small ones.

At the edges of the complex, convolutions at the interface between the dense gas and its moving ambient gas would be created and amplified by Kelvin-Helmholtz and Rayleigh-Taylor instabilities, and eventually long, thin tongues of dense gas should have formed (Woodward 1976).

So far, the picture we have just created should correspond to an outcome exactly opposite to what we observed, that is, high-density, rapidly moving gas on the outside of the complex, and lower density, undisturbed material well inside. At a much later time, however, the ambient pressure around the complex could relax significantly, allowing the compressed and stirred-up dense clumps near the surface to either re-expand or disperse. While the remaining material in the outer portions of the complex begins to settle down, the interior parts are still being agitated by the inward-moving shocks. Even after the shocks have collided and bounced, the accelerated clumps in the interior are not able to escape because of the presence of the overlying quiescent gas. As such clouds collide with each other, they will probably scatter, become fragmented, and generate secondary shocks and Alfvén waves.

Our model B indicates that the representative thermal pressures $p_h = n_h T_h$ within the small, high-velocity clouds are about twice as large as the pressures p_l for the larger, low-velocity ones. For an isothermal shock within the warm matrix at a temperature T_m, the time needed to reach the center is given by

$$t = 6.5 \times 10^6 \left(\frac{d}{100 \text{ pc}}\right)\left(\frac{p_l/p_h}{T_m/100 \text{ K}}\right)^{1/2} \text{ yr}$$

if the cloud complex is at a distance d and has a radius of 3°.5. For $p_h/p_l = 2$, $T_m = 100$ K, and $d = 130$ pc we find that $t \approx 6 \times 10^6$ yr, which means that the interior of the complex could still be at an elevated pressure which can prevent the small, rapidly moving clouds from expanding. This time scale is long compared with the time scale for H_2 formation of at most 10^6 yr in each of the clumps, and with the time scale of less than 10^5 yr for ultraviolet pumping.

If our interpretation of an isolated cloud complex and its recent history is correct, the phenomenon we are viewing may not be common. Our proposal implies that the center of the swarm of dense clouds is still in a state of agitation and enhanced pressures caused by an ancient, external disturbance, while the periphery has returned to a more quiescent state. It thus follows that the complex is being viewed at a special time. It would be interesting to see whether observations of rotationally excited H_2 at high resolution toward some other stars exhibit the same narrowing of the velocity profiles at higher J that we observed toward π Sco. If the phenomenon is commonplace, we would be forced to devise an explanation which has a more general foundation.

VIII. SUMMARY

a) Observations

The observations toward π Sco reported in this paper represent the highest resolution ultraviolet data obtained so far. The velocity resolution of about 2.4 km s^{-1} allows a detailed study of the H_2 line profiles for the first time. While each of our recorded profiles for transitions arising from rotational quantum numbers $J = 2$ to $J = 5$ appears to have a nearly symmetrical, single peak, a persistent disparity between the inferred optical depths of strong and weak lines (after compensating for the differences in transition probablilites) indicates that this peak is actually an assembly of very narrow features which are not resolved. Contrary to expectations, the profile widths appear to become narrower as J increases from 3 to 5. In addition, no systematic velocity difference in excess of 1 km s^{-1} was found between lines arising from rotational levels $J = 0$ to $J = 5$. While a small amount of CH^+ has been observed toward π Sco, our H_2 observations appear to disfavor a significant shocked component in the cloud, as well as the possibility that the high-J lines are formed in accelerating material at the edge of a circumstellar bubble around π Sco.

To prove that the interpretation of the deviations between the strong and weak lines could be explained by the assemblage of narrow components, we constructed a model for the appearance of various profiles for $J = 3$. We discovered that the number, widths, relative strengths, and placement of these components are remarkably well constrained by the observed profile shapes and the strength of the apparent optical depth anomaly, along with the requirement that the components be no narrower than thermal velocity spreads associated with the overall rotation temperature of 81 K between $J = 0$ and $J = 1$. Properties of the symmetrical arrangement of seven profiles are given in § IV*e*. Even though the actual profiles are slightly asymmetrical, we saw no value in complicating the model so that it would conform precisely.

b) Theoretical Models

Our strategy for explaining our results was to construct three steady state physical and chemical models for the gas, starting with (1) a simple, global interpretation to explain the populations in different J levels and the ratio $n(H_2)/n(H\ I)$, and then progressing to more elaborate pictures (2 and 3) to match the detailed profile phenomena discussed above. We summarize the three models as follows:

1. *Model H.*—This homogeneous model assumes that all of the atomic and molecular hydrogen is in a slab with a uniform total density and temperature. It is illuminated on one side by UV starlight which destroys some of the H_2 and also optically pumps some of the remaining molecules into high rotation states. We varied the incident UV intensity I_{UV} to obtain the best match with the observed relative populations in $J = 4$ and $J = 5$, and we used $N(H_2)$ in $J = 0$, 1, and 2 to constrain the temperature. The ratio $n(H_2)/n(H\ I)$ is governed by the local density and I_{UV}. Our model H with $n_H = 100$ cm^{-3}, $T = 81$ K, and $I_{UV} = 3$ times the average interstellar radiation field reproduced moderately well the observed $N(H_2\ J = 0$ to $J = 5)$ (plus upper limits for $J > 5$) and our estimate for $N(H\ I)$ which applies to the region containing the H_2.

2. *Clumpy model A.*—This model accounts for our observation that the profile we observed is actually composed of a nearly symmetrical arrangement of narrow, unresolved velocity components, rather than a monolithic profile from a single, uniform region having a turbulent velocity dispersion of several km s^{-1}. Here, we assumed that the clumps were arranged in such a way that the UV starlight can bathe them equally and that n_H is the same for each clump. Breaking the big slab into little clouds which do not shadow each other decreases the overall shielding and allows us to decrease I_{UV} to only 1.3 times the average field. We defined $N(H_2)$ in each clump to agree with the $J = 3$ profile model (Fig. 7). No significant change in n_H from model H was found. Temperatures for the low-velocity clumps near the center of the profile aggregate equaled 80 K, while for the outer profiles T needed to be reduced to about 40 K.

3. *Clumpy model B.*—Our problem with model A was that even though the predicted profile for $J = 3$ looked good (by design), profiles for $J = 2$ were too narrow, and those of $J = 4$ and $J = 5$ were too wide (Fig. 9). This behavior was a consequence of the decrease in pumping efficiency caused by the greater internal shielding within the low-velocity clouds which have higher column densities. As a result, there was proportionally more H_2 in higher J levels for the outlying components. To correct for this effect which contradicts the observations, we propose that the low-velocity clouds are arranged so that they block the radiation to the high-velocity ones. Even though the profiles for $J \geq 2$ do not overlap in velocity, the column densities in $J = 0$ and $J = 1$ at low velocities are sufficient to produce broad damping wings which can attenuate radiation in the lines which are important for pumping the high-velocity gas. We did not perform a precise calculation of the shielding for all modes of pumping; for simplicity we merely declared that each gas component was exposed to a different value of I_{UV}. The changed fluxes forced a big adjustment in total values of $N(H_2)$ for each component to get the correct $J = 3$ ratios from clump to clump. Table 11 shows the overall populations of H and H_2 plus other atomic and molecular species for models A and B, while Table 13 summarizes the differences between the two models for the apportionment of H_2 in specific J levels across different clumps. The general effect in going from model A to model B was to redistribute most of the H_2 from the central velocity components to the outer ones. Temperatures increased to 100 and 60 K for the low- and high-velocity components, respectively, and more reasonable fits to the data were obtained when n_H was reduced to 75 cm^{-3} at low velocities and raised to $n_H \gtrsim 300$ cm^{-3} for the outlying components. Model B seems to reproduce the observed abundances of some other species, such as HD, C I, CH, and CO, better than model A.

We had difficulty creating an explanation for the configuration described by model B that could apply to some generalized phenomenon that might be common to many H_2-bearing clouds in the interstellar medium. Instead, we propose a more specialized interpretation which may apply to a small gas complex in front of π Sco. This picture, supported by other observations, is that the material was subjected to a compression pulse when it was overtaken by a shock several million years ago. By now, the disturbed, high-velocity gas in small clumps near the surface of the complex have had enough time to disperse, but agitated gases in the center were created more recently by an inward-moving shock and are still trapped inside. Additional observational or theoretical inputs are needed to test this conjecture.

The observations reported in this paper came from a NASA sounding-rocket mission (27.082 UG) which represented both an end and a beginning: it was the last of over 2500 missions supported by personnel in the sounding-rocket group (Code 740) at the Goddard Space Flight Center at Greenbelt, Maryland, and it was the first successful flight of a new, specially built payload to study the interstellar medium. The IMAPS instrument was designed and constructed at the Ball Aerospace Systems Division (BASD) at Boulder, Colorado, under the direction of D. W. Simmons. Optical and detector system designs were carried out at BASD by M. Bottema and W. A. Delamere, respectively, while the detector electronics were created at Princeton by P. M. Zucchino and D. Long. G. R. Carruthers at the US Naval Research Laboratory provided crucial support with his ultraviolet sources and test equipment for our evaluation of the instrument's optics and detector. We thank J. H. Black for his critical reading of this paper and useful comments. This research was supported by NASA contract NAS5-26268 and grant NAG5-616 to Princeton University, and E. v.D. acknowledges support from NSF grant RII 86-20342. We are grateful to C. P. de Vries for obtaining the CH absorption-line spectra, and to J. E. Gunn for the use of his computer time, supported by NASA contract NAS5-25451.

REFERENCES

Aannestad, P. A., and Field, G. B. 1973, *Ap. J. (Letters)*, **186**, L29.
Allison, A. C., and Dalgarno, A. 1967, *Proc. Phys. Soc. London*, **90**, 609.
———. 1970, *Atomic Data*, **1**, 289.
Black, J. H., and Dalgarno, A. 1973, *Ap. J. (Letters)*, **184**, L101.
———. 1977, *Ap. J. Suppl.*, **34**, 405.
Black, J. H., and van Dishoeck, E. F. 1987, *Ap. J.*, **322**, 412.
Blades, J. C., Wynne-Jones, I., and Wayte, R. C. 1980, *M.N.R.A.S.*, **193**, 849.
Bohlin, R. C., Hill, J. K., Jenkins, E. B., Savage, B. D., Snow, T. P., Spitzer, L., and York, D. G. 1983, *Ap. J. Suppl.*, **51**, 277.
Bohlin, R. C., Savage, B. D., and Drake, J. F. 1978, *Ap. J.*, **224**, 132.
Cappa de Nicolau, C. E., and Pöppel, W. G. L. 1986, *Astr. Ap.*, **164**, 274.
Carruthers, G. R., and Opal, C. B. 1985, *Adv. Electronics Electron Phys.*, **64B**, 299.
Crawford I. A., Barlow, M. J., and Blades, J. C. 1989, *Ap. J.*, **336**, 212.
Dabrowski, I. 1984, *Canadian J. Phys.*, **62**, 1639.
Dalgarno, A., Black, J. H., and Weisheit, J. C. 1973, *Ap. Letters*, **14**, 77.
Danks, A. C., Federman, S. R., and Lambert, D. L. 1984, *Astr. Ap.*, **130**, 62.
de Geus, E. J. 1988, Ph.D. thesis, University of Leiden.
de Geus, E. J., Bronfman, L., and Thaddeus, P. 1988, *Astr. Ap.*, submitted.
de Geus, E. J., de Zeeuw, P. T., and Lub, J. 1988, *Astr. Ap.*, in press.
Draine, B. T. 1978, *Ap. J. Suppl.*, **36**, 595.
Draine, B. T., and Katz, N. S. 1986, *Ap. J.*, **306**, 655.
Duley, W. W., and Williams, D. A. 1986, *M.N.R.A.S.*, **223**, 177.
Elitzur, M., and Watson, W. D. 1978, *Ap. J. (Letters)*, **222**, L141.
———. 1980, *Ap. J.*, **236**, 172.
Federman, S. R., Glassgold, A. E., Jenkins, E. B., and Shaya, E. J. 1980, *Ap. J.*, **242**, 545.
Ford, A. L. 1975, *J. Molec. Spectrosc.*, **56**, 251.
Green, S., and Truhlar, D. G. 1979, *Ap. J. (Letters)*, **231**, L101.
Hobbs, L. M. 1969, *Ap. J.*, **157**, 135.
———. 1974, *Ap. J.*, **191**, 381.
———. 1976, *Ap. J.*, **203**, 143.
Horne, K. 1986, *Pub. A.S.P.*, **98**, 609.
Jenkins, E. B., Joseph, C. L., Long, D., Zucchino, P. M., Carruthers, G. R., Bottema, M., and Delamere, W. A. 1988, *Ultraviolet Technology II* (*Proc. S.P.I.E.*, **932**, 213).
Jenkins, E. B., and Shaya, E. J. 1979, *Ap. J.*, **231**, 55.
Jura, M. 1975*a*, *Ap. J.*, **197**, 575.
———. 1975*b*, *Ap. J.*, **197**, 581.
———. 1980, *Ap. J.*, **235**, 63.
Knapp, G. R., and Bowers, P. F. 1988, *Ap. J.*, **331**, 974.
Kurucz R. L., and Peytremann, E. 1975, *A Table of Semiempirical gf Values, Part I* (SAO Spec. Rept. 362; Cambridge: Smithsonian Inst. Astr. Obs.).
Lambert, D. L., and Danks, A. C. 1986, *Ap. J.*, **303**, 401.
Lampton, M., Margon, B., and Bowyer, S. 1976, *Ap. J.*, **208**, 177.
Langer, W. D., Glassgold, A. E., and Wilson, R. W. 1987, *Ap. J.*, **322**, 450.
Leonas, V. B., and Pjarnpuu, A. A. 1981, *Soviet Astr. Letters*, **7**, 19.
Lepp, S., Dalgarno, A., van Dishoeck, E. F., and Black, J. H. 1988, *Ap. J.*, **329**, 418.
Marschall, L. A., and Hobbs, L. M. 1972, *Ap. J.*, **173**, 43.
Meyer, C. F. 1949, *The Diffraction of Light, X-Rays, and Material Particles* (2d ed.; Ann Arbor: Edwards.), chap. 6, § 41.
Moore, C. E. 1975, *Selected Tables of Atomic Spectra* (NSRDS–NBS 3, Sec. **5**).
———. 1976, *Selected Tables of Atomic Spectra* (NSRDS–NBS 3, Sec. **7**).
Morton, D. C. 1975, *Ap. J.*, **197**, 85.
Morton, D. C., and Dinerstein, H. L. 1976, *Ap. J.*, **204**, 1.
Mosteller, F., and Tukey, J. W. 1977, *Data Analysis and Regression* (Reading: Addison-Wesley), chap. 10.
Pineau-des Forêts, G., Flower, D. R., Hartquist, T. W., and Dalgarno, A. 1986, *M.N.R.A.S.*, **220**, 801.
Roberge, W. G., Dalgarno, A., and Flannery, B. P. 1981, *Ap. J.*, **243**, 817.
Roueff, E. 1988, in *Rate Coefficients in Astrochemistry*, ed. T. J. Millar and D. A. Williams (Dordrecht: Kluwer), p. 135.
Savage, B. D., Bohlin, R. C., Drake, J. F., and Budich, W. 1977, *Ap. J.*, **216**, 291.
Sharpless, S. 1959, *Ap. J. Suppl.*, **4**, 257.
Snow, T. P. 1983, *Ap. J. (Letters)*, **269**, L57.

Snow, T. P., McClintock, W. E., and Voels, S. A. 1988, *Ap. J.*, **325**, 402.
Spitzer, L., and Cochran, W. D. 1973, *Ap. J. (Letters)*, **186**, L23.
Spitzer, L., Cochran, W. D., and Hirshfeld, A. 1974, *Ap. J. Suppl.*, **28**, 373.
Spitzer, L., and Morton, W. A. 1976, *Ap. J.*, **204**, 731.
Spitzer, L., and Zweibel, E. G. 1974, *Ap. J. (Letters)*, **191**, L127.
van Dishoeck, E. F., and Black, J. H. 1986, *Ap. J. Suppl.*, **62**, 109 (vDB).
van Dishoeck, E. F., and Black, J. H. 1988*a*, *Ap. J.*, **334**, 771.
———. 1988*b*, in *Rate Coefficients in Astrochemistry*, ed. T. J. Millar and D. A. Williams (Dordrecht: Kluwer), p. 209.
Viala, Y. P., Roueff, E., and Abgrall, H. 1988, *Astr. Ap.*, **190**, 215.
Woodward, P. R. 1976, *Ap. J.*, **207**, 484.

EDWARD B. JENKINS and JOANNA F. LEES: Princeton University Observatory, Princeton, NJ 08544-1001

EWINE F. VAN DISHOECK: Division of Geological and Planetary Sciences, Caltech 170-25, Pasadena, CA 91125

ERIC M. WILCOTS: Department of Astronomy FM-20, University of Washington, Seattle, WA 98195

1989ApJ...343..785J

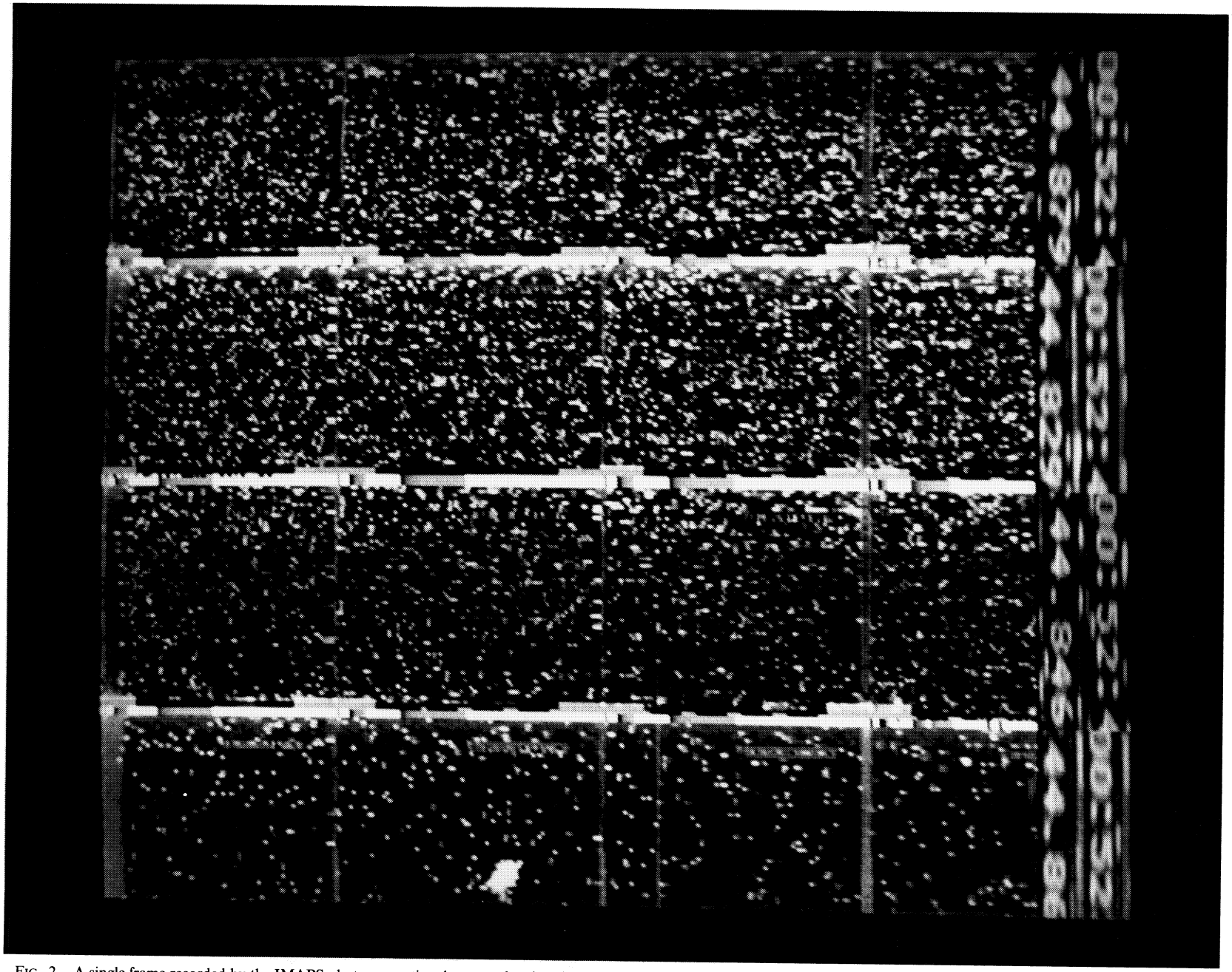

FIG. 2.—A single frame recorded by the IMAPS photon-counting detector, showing single photoevents. Interruptions in the video signal result in the frame being divided into 16 panels. (The losses of picture area are not proportional to the widths of the partitions, since the CCD charge clocking was momentarily halted during each pause in the signal.) Small rectangles with anomalous patterns in the top right-hand portion of each panel are caused by the insertion of timing signals for identifying the frames when they are digitized from the analog VCR tape after the flight. Echelle orders can be barely discerned in the pattern of photoevents. The bright spot at the bottom of the frame is the broad-band image of the star used for tracking the changes in rocket pointing.

1989ApJ...343..785J

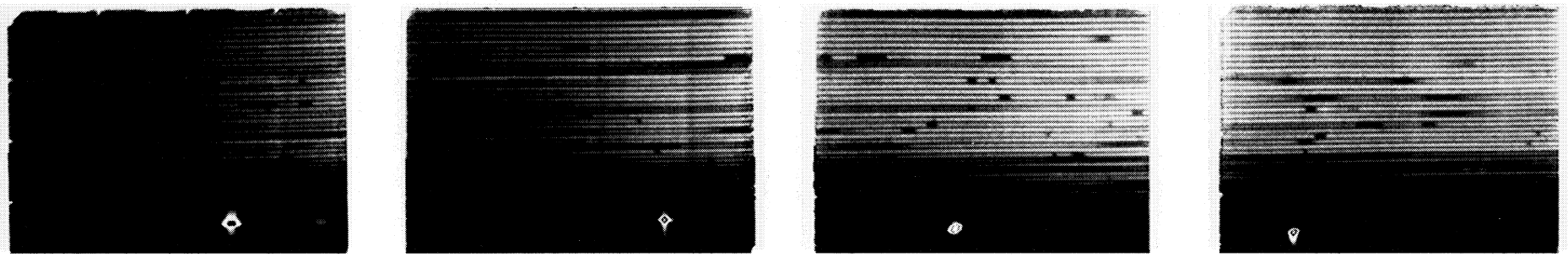

FIG. 3.—Composite images of the spectrum for each of the four echelle tilt angles, arranged to show the complete free spectral range of the echelle orders